Official Journal of Turkish Society of Magnetic Resonance

CRMRI

Current Research in MRI

Early and Persistent White Matter Damage in Severe Traumatic Brain Injury: A Longitudinal Diffusion Tensor Imaging Analysis

Barış Genç, Kerim Aslan, Lütfi İncesu

Effectiveness of Diffusion-Weighted Magnetic Resonance Imaging in Differentiating Mediastinal Lymphadenopathy

Türkhun Çetin, Fulya Memiş

Branch-to-Total Pulmonary Artery Area Ratio as a Predictor of Flow Limitation in Tetralogy of Fallot: MRA and Phase Contrast MRI Study

Ali Fuat Tekin, Tuba Banaz, Ömer Altun, Berk Tütüncüoğlu, Muhammed Faruk Kazanbaş, Mehmet Kadıoğlu, Mustafa Kan, Yiğit Can Kartal, İlker Kemal Yücel, Serçin Özkök

Assessment of Meniscal Pathologies and Meniscal Volume Quantification in Individuals with and without Radiographic Osteoarthritis

Özge Tanişman, Eren Tobcu, Bilgin Topcu, Erdal Karavaş

AVES

curremr.com

TMRD
TÜRK MANYETİK
REZONANS DERNEĞİ
TURKISH SOCIETY
OF MAGNETIC RESONANCE

Current Research in MRI

Current Research in MRI

About the Current Research in MRI

Current Research in MRI is a peer reviewed, open access, on-line-only journal published by the Turkish Society of Magnetic Resonance.

Current Research in MRI is a triannual journal that is published in English in April, August, and December.

Indexing
Current Research in MRI is covered in the following indexing database;

- EBSCO
- DOAJ
- China National Knowledge Infrastructure (CNKI)

All content published in the journal is permanently archived in Portico.

Aims, Scope, and Audience
Current Research in MRI aims to publish studies of the highest scientific and clinical value. It also encourages the submission of high-quality research in the field of radiology.

Current Research in MRI covers a wide range of topics related to radiology.

Current Research in MRI publishes original articles, reviews, case reports, and letters to the editor that are prepared in accordance with ethical guidelines.

The target audience of the journal includes healthcare professionals, physicians, and researchers who are interested in or working in the field of radiology.

You can reach the current version of the instructions to authors at https://curremr.com/EN

Current Research in MRI

CONTENTS

Original Article

Early and Persistent White Matter Damage in Severe Traumatic Brain Injury: A Longitudinal Diffusion Tensor Imaging Analysis

Barış Genç[1], Kerim Aslan[2], Lütfi İncesu[3]

[1]Department of Radiology, Ondokuz Mayıs University School of Medicine, Samsun, Türkiye
[2]Department of Neuroradiology, Ondokuz Mayıs University School of Medicine, Samsun, Türkiye
[3]Department of Radiology, Ondokuz Mayıs University School of Medicine, Samsun, Türkiye

Abstract

Objective: This study aims to identify early and longitudinal microstructural changes in white matter tracts in patients with severe traumatic brain injury (TBI) using tract-based spatial statistics (TBSS) and fully automated tractographic methods.

Methods: Participants were 16 adult TBI patients with a Glasgow Coma Scale (GCS) score <7 and 16 age- and gender-matched healthy controls. Magnetic resonance imaging (MRI) scans were performed using a 3 Tesla scanner, following the high-angular resolution diffusion imaging (HARDI) protocol. Diffusion tensor imaging (DTI) parameters [fractional anisotropy (FA), mean diffusivity (MD), radial diffusivity (RD), and axial diffusivity (AD)] were calculated. TractSeg was used for automated segmentation of white matter tracts, including the arcuate fasciculus (AF), anterior thalamic radiation (ATR), corpus callosum, cingulum, corticospinal tract (CST), superior longitudinal fasciculus (SLF), and inferior longitudinal fasciculus (ILF). Statistical comparisons between groups and longitudinal analyses within the patient group were conducted using *t*-tests and Wilcoxon signed-rank tests, with significance thresholds adjusted for multiple comparisons.

Results: In the acute phase, TBSS revealed widespread decreases in FA and AD, and increases in MD and RD in several white matter tracts including the ATR, CST, cingulum, and corpus callosum. Tractography also showed decreased FA and increased RD and MD in several tracts. Longitudinal analysis indicated persistent decreases in FA and increases in RD over time, while tractography did not show significant longitudinal changes.

Conclusion: The study demonstrates significant early white matter damage in severe TBI patients, with continued microstructural changes observed longitudinally.

Keywords: Diffusion tensor imaging (DTI), longitudinal analysis, tract-based spatial statistics (TBSS), traumatic brain injury (TBI), white matter microstructure

INTRODUCTION

Traumatic brain injury (TBI) is a significant cause of morbidity and mortality in young patients.[1] Diffuse axonal injury involves axonal disruptions in trauma patients and may not be visible on computed tomography or conventional magnetic resonance imaging (MRI) sequences if there is no accompanying hemorrhage. Diffusion-weighted imaging (DWI) has become widely used in recent years for its ability to demonstrate microstructural changes in tissues not detectable on conventional MRI.[2] Diffusion tensor imaging (DTI) allows for the visualization of white matter tracts by altering diffusion gradients in specific directions. Fractional anisotropy (FA) is 1 of the key parameters of DTI, providing highly sensitive information about the integrity of white matter tracts. The literature indicates that DTI can detect microstructural abnormalities in TBI that are not apparent on conventional MRI sequences, with studies spanning at least 20 years. These studies have shown decreases in FA and increases in mean diffusivity (MD) in these patients, particularly in commissural fibers such as the corpus callosum.[3] Diffusion tensor imaging has successfully revealed microstructural changes in mild, moderate, and severe TBI.[4,5]

Trauma is a process that triggers neuroinflammation. Encephalomalacia and gliosis develop in these patients, and increased neuroinflammation can exacerbate the existing brain injury. Therefore, identifying microstructural changes in the chronic phase of TBI is crucial for patient management.[6] However, there are very few longitudinal studies investigating microstructural changes in TBI. In the existing studies, the focus has primarily been on mild TBI.[7] Furthermore, the degree of neuroinflammation in mild TBI is not the same as in severe TBI.[8] Thus, studying longitudinal changes in severe TBI is of significant importance.

Several methods exist to investigate microstructural changes in tissues using DTI. The traditional region of interest (ROI) method involves marking specific areas using certain atlases and examining the average DTI parameters in these regions. Studies using this method in TBI have found widespread decreases in FA and increases in MD, particularly in areas where commissural fibers pass.[9,10] However, this method is dependent on the observer and only includes measurements from specific white matter regions.[11] Another method, tract-based spatial statistics (TBSS), is largely user-independent and allows for voxel-wise group comparisons across the entire brain by automatically transferring white

matter tracts onto a white matter skeleton and taking local maxima.[12] Tract-based spatial statistics has become a popular alternative to the ROI method because it mitigates some of the subjective elements involved in manual ROI selection. By projecting all participants' white matter tracts onto a common skeleton, TBSS enables a more standardized comparison across subjects, facilitating voxel-wise statistical analyses of the entire brain. Many studies have shown microstructural changes throughout the brain in TBI using TBSS.[13] However, TBSS can introduce bias through statistical measurements taken at local maxima and may produce incorrect calculations in crossing fibers.[14]

Another advantage of DTI is its non-invasive ability to visualize white matter tracts, which is particularly useful in preoperative planning for tumor patients. Traditional DTI typically employs a maximum b-value between 800 and 1000 s/mm². However, this b-value range has limitations, particularly when it comes to accurately depicting complex fiber configurations such as crossing or kissing fibers. Lower b-values may result in a loss of directional information in regions with complex fiber architecture, leading to inaccuracies in tractography, especially in areas like the centrum semiovale where multiple fiber bundles intersect.[15] Recently, the use of high-angular resolution diffusion imaging (HARDI) with higher b-values and constrained spherical deconvolution (CSD) has been shown to produce better results compared to classical tractography using lower b-values.[16] Identifying white matter tracts traditionally involves a labor-intensive process requiring manual selection of multiple parameters, including start and end points and voxel transition angles, which depends heavily on the operator's experience. Recently developed deep learning-based algorithms, such as TractSeg using CSD, can automatically segment white matter tracts.[17] There are a lot of studies in the literature investigating tractographic changes in TBI, and most of these studies have utilized classical DTI techniques.[18] A recent study demonstrated that tractography using CSD might better reveal changes in TBI compared to classical tractography methods.[19] However, the number of studies investigating tractographic changes in TBI using CSD-based tractography is quite limited.

Our study has several objectives. First, the aim is to reveal early microstructural changes in the white matter of patients with severe TBI (Glasgow Coma Scale [GCS] < 7) using TBSS and fully automatic tractographic methods. Our second objective is to identify longitudinal microstructural changes in these patients.

MAIN POINTS

- This study reveals significant early microstructural damage in the white matter tracts of severe TBI patients, with notable decreases in fractional anisotropy (FA) and axial diffusivity (AD), and increases in mean diffusivity (MD) and radial diffusivity (RD).
- Longitudinal analysis indicates persistent and progressive white matter damage over time, characterized by continued decreases in FA and increases in RD, underscoring the chronic nature of brain injury in severe TBI patients.
- Tract-based spatial statistics (TBSS) effectively detected both acute and chronic microstructural changes, while constrained spherical deconvolution (CSD)-based tractography proved more sensitive to acute damage, highlighting the importance of advanced imaging techniques for comprehensive TBI assessment.

MATERIAL AND METHODS
Participants
This observational study utilized clinical and MRI images licensed under the Creative Commons Attribution 4.0 International (CC-BY 4.0) from a public dataset (https://openneuro.org/datasets/ds003367).[20] Ethics committee approval was received from the "blinded for review" Ondokuz Mayıs University Clinical Research Ethics Committee (Approval No: OMUKAEK 2024295 Date: 5/7/2024). The cohort included 16 adult patients with TBI, a GCS score of less than 7, who did not open their eyes and completely recovered from this coma state after 6 months (Age [Median: 27.5; Inter Quantile Range (IQR): 21.5-33], Gender [12 Male, 4 Female]), and 16 age- and gender-matched healthy controls (Age [Median: 27; IQR: 21-35], Gender [12 Male, 4 Female]). Follow-up MRI examinations were available for 9 of these patients (Median: 206 [190-370] days). All subjects consisted of individuals who did not have a pre-existing neurodegenerative disease or a history of TBI.[20,21] Informed consent was obtained from participants by researchers while collecting data within the scope of the open science project. The findings are presented in accordance with the strengthening the reporting of observational studies in epidemiology (STROBE) guidelines.[22]

MRI Acquisition and Preprocessing
Magnetic resonance imaging scans were performed using a Siemens 3 Tesla Skyra device with a 32-channel head coil. Following the HARDI protocol, 60 slices (b=2000 s/mm²) and 10 slices with b=0 were acquired with a thickness of 2 mm. Other sequence parameters were defined as per previous literature.[21]

Initially, an average b=0 image was generated from the diffusion images, and a brain tissue mask was created using SynthStrip.[23] Eddy current artifact and motion artifact corrections were applied using FMRIB Software Library (FSL) eddy.[24] Images were aligned to the Montreal Neurological Institute (MNI-152) template, and FA, MD, radial diffusivity (RD), and axial diffusivity (AD) maps were generated using FSL dti_fit. All FA and MD images were evaluated by a radiologist with 8 years of experience.

Preprocessed diffusion-weighted images were analyzed using TractSeg, which performed fully automated segmentation of key white matter tracts, including the arcuate fasciculus (AF), anterior thalamic radiation (ATR), corpus callosum, cingulum, corticospinal tract (CST), superior longitudinal fasciculus (SLF), and inferior longitudinal fasciculus (ILF) (Figure 1).[17] For each segmented tract, the average values of FA, MD, AD, and RD were automatically calculated using the fslstats tool.[25]

Statistical Analysis
Tract-Specific Analysis
For the comparison of FA, MD, RD, and AD values in the tracts segmented by TractSeg between the early period of the patient group and the control group, either the *t*-Test or the Mann–Whitney *U* test was used, depending on the normality of the distribution. For the comparison of early and late findings within the patient group, either the paired *t*-test or the Wilcoxon signed-rank test was employed based on the distribution. Given that 32 parameters were investigated for each individual, the alpha threshold was set at 0.05/32, which is approximately 0.0016.

Tract-Based Spatial Statistics
In accordance with the main TBSS pipeline (https://fsl.fmrib.ox.ac.uk/fsl/fslwiki/TBSS/UserGuide),[12] FA images were aligned to the MNI
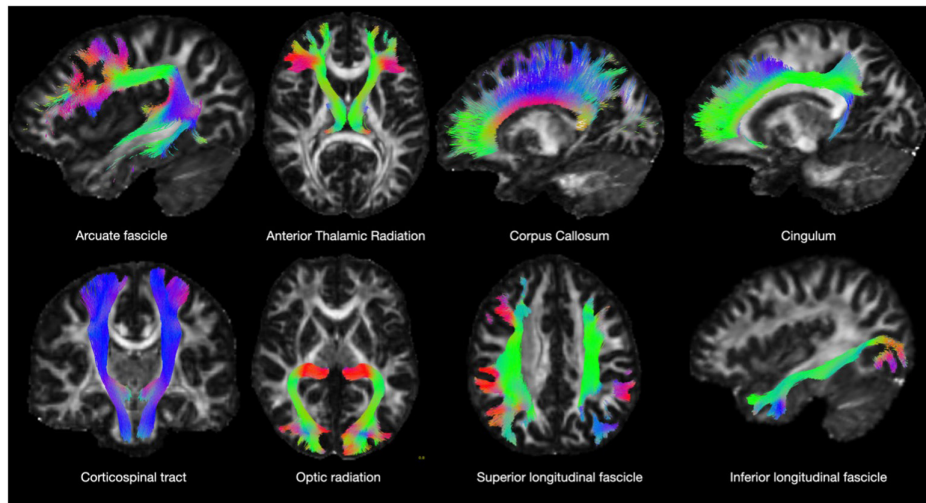
Figure 1. White matter tracts segmented using TractSeg (images from sub-TCRc007).

template and subsequently to the FMRIB-58 FA template. Average FA skeleton images were then created. Differences between the patient and control groups were assessed using a *t*-test, and longitudinal changes were evaluated using a paired *t*-test. To determine the significance of threshold-free cluster enhancement, a Monte Carlo simulation with n=5000 iterations was performed.[26] A *P*-value of less than .05 was considered statistically significant. Tracts showing significant differences were identified using the Johns Hopkins University (JHU) white matter atlas Tractography Atlas within FSL's autoaq.[27]

RESULTS
Cross-Sectional Analysis
Tract-Based Spatial Statistics (TBSS)
Our TBSS results indicate widespread decreases in FA (Minimum $P = .002$) and AD (Minimum $P = .002$), along with increases in MD (Minimum $P = .004$) and RD (Minimum $P = .002$) in traumatic coma patients. These changes were observed bilaterally in the ATR, CST, cingulum, forceps major and minor, OR, ILF, SLF, and UF (Figure 2).
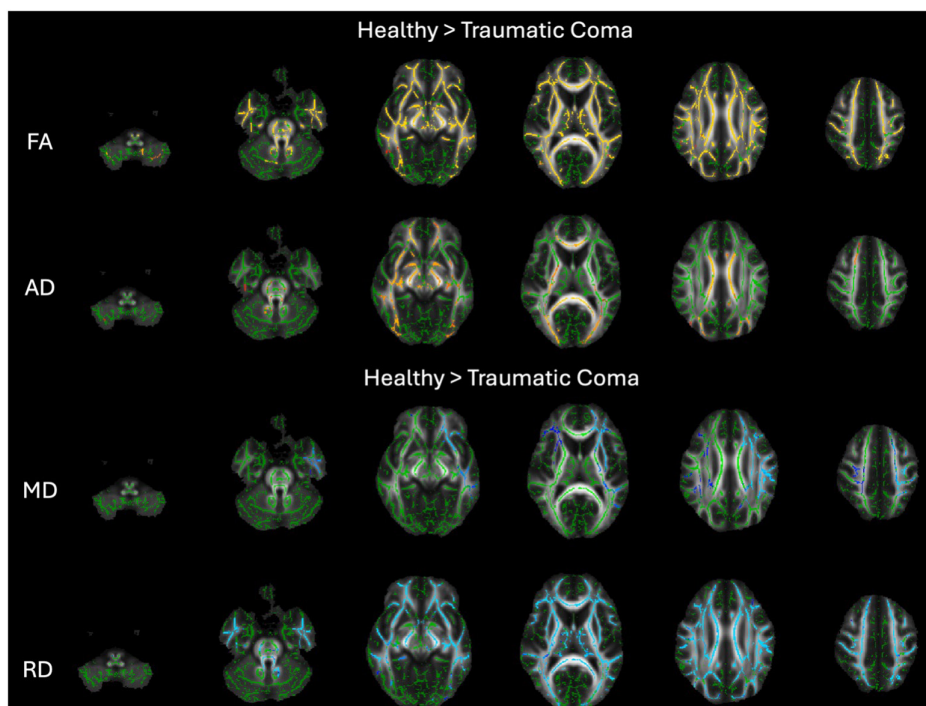
Figure 2. White matter tracts showing changes in early post-traumatic brain injury patients compared to healthy controls according to TBSS (P < .05). AD, axial diffusivity; FA, fractional anisotropy; MD, mean diffusivity; RD, radial diffusivity; TBSS, tract-based spatial statistics.

Tractography Findings
According to the tractography results, there was a decrease in FA observed in the bilateral AF, CST, ATR, cingulum, SLF, UF, and corpus callosum fibers. An increase in MD was found in the left AF, bilateral ATR, and left UF fibers. Additionally, there was an increase in RD detected in the bilateral AF, bilateral ATR, bilateral cingulum, corpus callosum, and bilateral UF fibers ($P < .0016$). No significant changes in AD were observed between the groups in the identified white matter tracts (Figure 3).

Longitudinal Analysis
Tract-Based Spatial Statistics
In the longitudinal analysis, over time, there was a decrease in FA (minimum $P = .026$) and an increase in RD (minimum $P = .022$) observed in the white matter tracts, including the bilateral ATR, bilateral CST, bilateral cingulum, forceps major and minor, bilateral Inferior Frontoccipital Fasciculus (IFOF), bilateral ILF, and bilateral SLF fibers (Figure 4). A more limited area showed an increase in MD (minimum $P = .028$). Axial diffusivity did not show any changes over time.

Longitudinal Analysis
Tractography Findings
In the longitudinal analysis, no significant differences were observed in the white matter tracts.

DISCUSSION
This study investigated the acute and chronic changes in the brains of patients in comas with severe TBI. Our findings demonstrate widespread decreases in FA and AD, and increases in MD and RD in white matter areas in the acute phase of severe traumatic coma, as revealed by TBSS analysis. Tractography analysis also indicated reduced FA and increased RD and MD along white matter tracts in these patients. Longitudinal analysis revealed that this white matter damage continued progressively even after the patients regained consciousness.

Diffusion tensor imaging changes in TBI have been a subject of research for many years.[3] Previous studies have similarly shown that DTI is a sensitive method for detecting TBI. Fractional anisotropy, the most commonly used parameter in DTI, showed widespread reduction in the acute phase in our study, consistent with the literature.[28,29] The non-specific decrease in FA can be due to myelin loss, axonal loss, or crossing fibers.[30] Experimental studies in rats have suggested that RD could be a specific indicator of myelin integrity.[31] As myelin integrity decreases, water molecules diffuse more in directions other than the primary fiber orientation. Studies have shown that an increase in RD, consistent with myelin damage, has been present since the early stages of trauma, and these findings are consistent with our study.[32,33] Mean diffusivity is also a non-specific parameter affected by many factors disrupting fiber integrity. Similar to the literature, our study found widespread increases in MD in TBI, indicating early axonal and myelin loss.[3]

Traumatic brain injury is not just an acute process. A study in mice showed early post-trauma axonal damage, microglia and astrocyte activation, and early axonal damage associated with decreased AD, consistent with our study.[34] In the chronic phase, neuroinflammation increases, leading to axonal degeneration, more pronounced demyelination, and gliosis.[34] Palacios et al's[7] study in patients with mild TBI found widespread FA decreases and MD increases early after trauma, similar to our study, but no FA and MD changes in longitudinal analysis. However, that study showed longitudinal increases in neurite density index and free water fraction from Neurite Orientation Dispersion and Density Imaging (NODDI) parameters. NODDI is more sensitive to microstructural changes than conventional DTI.[35] In the study conducted by Veeramuthu and colleagues on patients with mild TBI, a decrease in FA along with an increase in MD and RD was detected in the early stages of TBI. Similar to our study, the longitudinal analysis demonstrated that the progressive decrease in FA and the increase in MD and RD continued.[33] A recent study shows that there
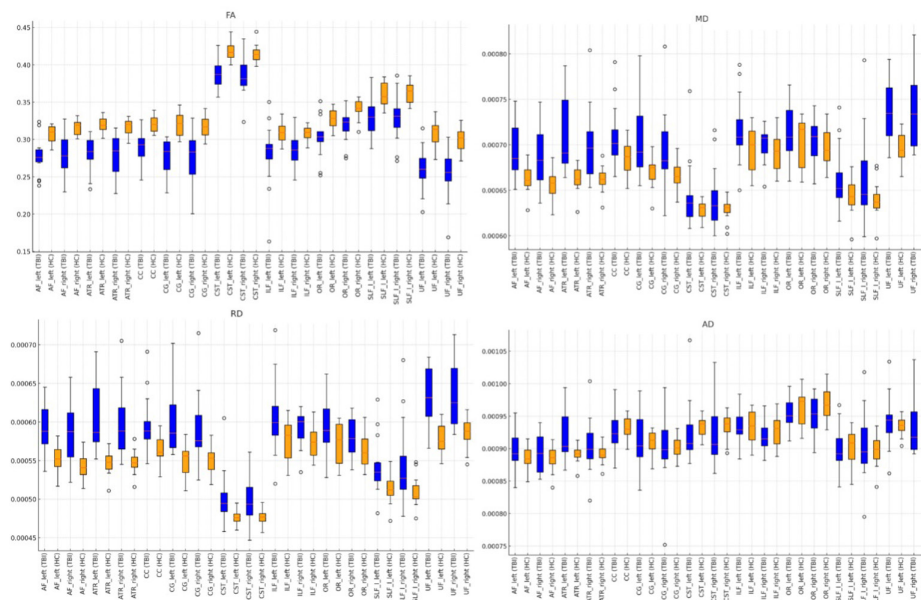
Figure 3. Box-plot representation of changes in FA, MD, RD, and AD in white matter tracts segmented by tract-specific statistics in the early period of trauma. AD, axial diffusivity; AF, arcuate fasciculus; CG, cingulum; CST, corticospinal tract; FA, fractional anisotropy; HC, healthy control; ILF, inferior longitudinal fasciculus; MD, mean diffusivity; OR, optic radiation; RD, radial diffusivity; SLF, superior longitudinal fasciculus; TBI, traumatic brain injury; UF, uncinate fasciculus.
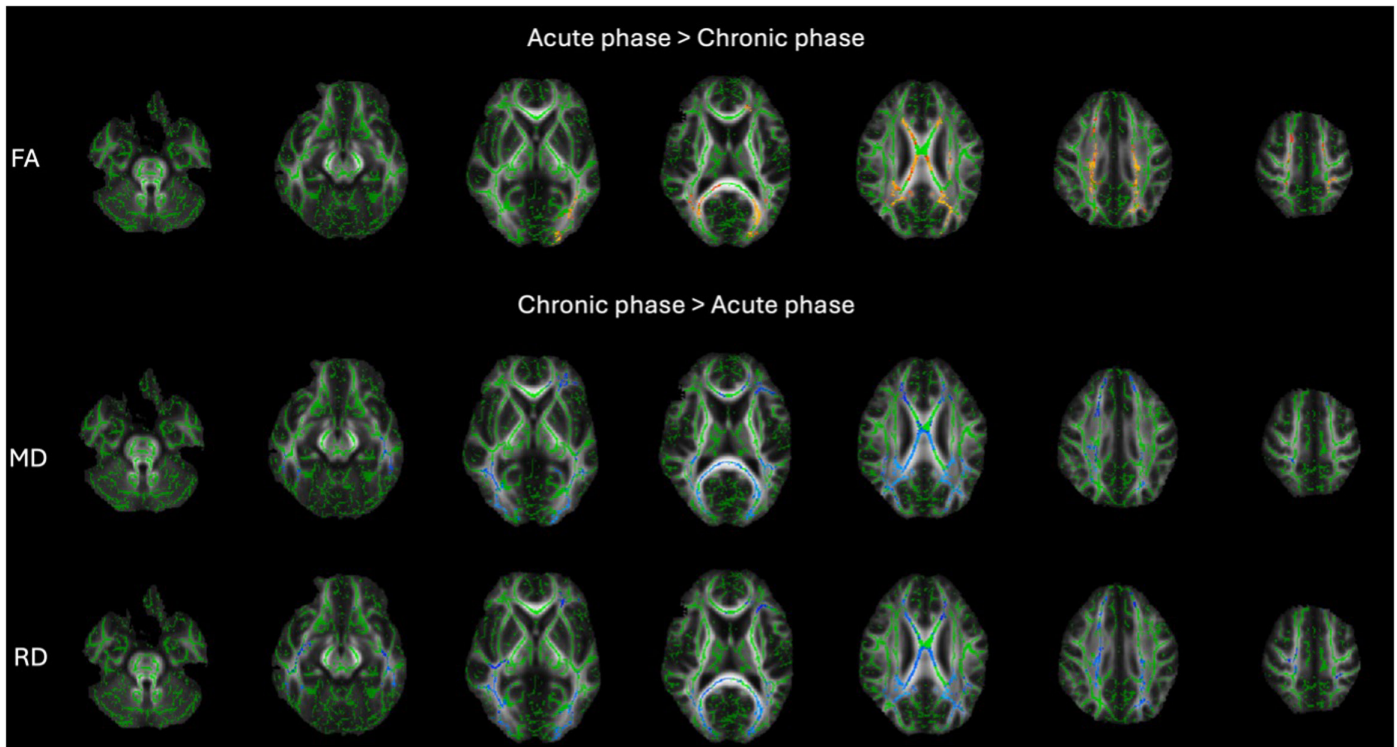
Figure 4. White matter tracts showing changes longitudinally in longitudinally post-traumatic brain injury patients according to TBSS (P < .05). AD, axial diffusivity; FA, fractional anisotropy; MD, mean diffusivity; RD, radial diffusivity; TBSS, tract-based spatial statistics.

is a longitudinal increase in enlarged perivascular spaces in patients with TBI, along with a longitudinal increase in the DTI-ALPS index.[36] These combined findings indicate that microstructural changes in trauma patients continue longitudinally.

The optimal tractographic algorithm for investigating microstructural changes in TBI is not yet clearly established.[37] Tallus et al's[19] study showed that using CSD-based tractographic methods, as in our study, rather than classical tractographic methods, is more successful in revealing tractographic changes in TBI. However, that study did not use b-values compatible with HARDI. Our study used a tractographic algorithm with b-values compatible with HARDI. Therefore, CSD-based tractography using high b-values is useful in detecting acute traumatic injury. However, AD decreases, an indicator of acute traumatic axonal injury, were not shown with CSD-based tractography, but were detected with TBSS. Additionally, longitudinal changes detected with TBSS were not shown with CSD-based tractography. Future studies using multi-shell multi-tissue spherical convolution tractography may address these limitations.

Most studies to date have focused on microstructural changes in mild TBI. However, our study shows that progressive white matter damage continues in severe head trauma. Despite clinical improvement, progressive demyelinating processes and gliosis continue, and voxel-based analysis methods like TBSS may be useful in tracking these processes.

Our study has several limitations. First, it is based on data shared for use by all scientists through the open science project, leading to limited patient data. Clinical examination findings of the patients were not available, so DTI findings could not be correlated with cognitive data. The small number of patients makes it difficult to generalize these findings. However, our study may pave the way for large-scale multicenter studies in the future. Despite using DTI-based tractography, incorporating multi-shell b-values, NODDI, diffusion kurtosis, and other advanced DTI methods could deepen our findings.

In conclusion, our study shows that early axonal loss and changes consistent with myelin damage occur in TBI. Even after patients regain consciousness, gliotic processes, neuroinflammation, and demyelinating processes in the brain continue in the long term. While CSD-based tractography methods are useful for assessing acute damage, TBSS is successful in evaluating both acute and chronic damage.

REFERENCES

1. Capizzi A, Woo J, Verduzco-Gutierrez M. Traumatic brain injury: an overview of epidemiology, pathophysiology, and medical management. *Med Clin North Am*. Medical Clinics. 2020;104(2):213-238. [CrossRef]

2. Paszkowska E, Wasilewski G, Szalcunas-Olsztyn A, Jancewicz P, Stefanowicz E. The comparison of the value of ct imaging and selected MRI sequences (including DWI) in the evaluation of axonal injuries. *Pol J Radiol*. 2010;75(1):13-17.

3. Hulkower MB, Poliak DB, Rosenbaum SB, Zimmerman ME, Lipton ML. A decade of DTI in traumatic brain injury: 10 years and 100 articles later. *AJNR Am J Neuroradiol*. 2013;34(11):2064-2074. [CrossRef]

4. Shenton ME, Price BH, Levin L, Edersheim JG. Mild traumatic brain injury: is DTI ready for the courtroom? *Int J Law Psychiatry*. 2018;61:50-63. [CrossRef]

5. Kennedy MRT, Wozniak JR, Muetzel RL, et al. White matter and neurocognitive changes in adults with chronic traumatic brain injury. *J Int Neuropsychol Soc*. 2009;15(1):130-136. [CrossRef]

6. Xiong Y, Mahmood A, Chopp M. Current understanding of neuroinflammation after traumatic brain injury and cell-based therapeutic opportunities. *Chin J Traumatol*. 2018;21(3):137-151. [CrossRef]

7. Palacios EM, Owen JP, Yuh EL, et al. The evolution of white matter microstructural changes after mild traumatic brain injury: a longitudinal DTI and NODDI study. *Sci Adv*. 2020;6(32):eaaz6892. [CrossRef]

8. Simon DW, McGeachy MJ, Bayır H, Clark RSB, Loane DJ, Kochanek PM. The far-reaching scope of neuroinflammation after traumatic brain injury. *Nat Rev Neurol*. 2017;13(3):171-191. [CrossRef]

9. Yuan W, Holland SK, Schmithorst VJ, et al. Diffusion tensor MR imaging reveals persistent white matter alteration after traumatic brain injury experienced during early childhood. *AJNR Am J Neuroradiol*. 2007;28(10):1919-1925. [CrossRef]

10. Kim E, Yoo RE, Seong MY, Oh BM. A systematic review and data synthesis of longitudinal changes in white matter integrity after mild traumatic brain injury assessed by diffusion tensor imaging in adults. *Eur J Radiol*. 2022;147:110117. [CrossRef]

11. Lilja Y, Gustafsson O, Ljungberg M, Nilsson D, Starck G. Impact of region-of-interest method on quantitative analysis of DTI data in the optic tracts. *BMC Med Imaging*. 2016;16(1):42. [CrossRef]

12. Smith SM, Jenkinson M, Johansen-Berg H, et al. Tract-based spatial statistics: voxelwise analysis of multi-subject diffusion data. *Neuroimage*. 2006;31(4):1487-1505. [CrossRef]

13. Abdullah AN, Ahmad AH, Zakaria R, et al. Disruption of white matter integrity and its relationship with cognitive function in non-severe traumatic brain injury. *Front Neurol*. 2022;13:1011304. [CrossRef]

14. Bach M, Laun FB, Leemans A, et al. Methodological considerations on tract-based spatial statistics (TBSS). *Neuroimage*. 2014;100:358-369. [CrossRef]

15. Jeurissen B, Leemans A, Tournier JD, Jones DK, Sijbers J. Investigating the prevalence of complex fiber configurations in white matter tissue with diffusion magnetic resonance imaging. *Hum Brain Mapp*. 2013;34(11):2747-2766. [CrossRef]

16. Jeurissen B, Tournier JD, Dhollander T, Connelly A, Sijbers J. Multi-tissue constrained spherical deconvolution for improved analysis of multi-shell diffusion MRI data. *Neuroimage*. 2014;103:411-426. [CrossRef]

17. Wasserthal J, Neher P, Maier-Hein KH. TractSeg-Fast and accurate white matter tract segmentation. *Neuroimage*. 2018;183:239-253. [CrossRef]

18. Wang JY, Bakhadirov K, Devous MD, et al. Diffusion tensor tractography of traumatic diffuse axonal injury. *Arch Neurol*. 2008;65(5):619-626. [CrossRef]

19. Tallus J, Mohammadian M, Kurki T, Roine T, Posti JP, Tenovuo O. A comparison of diffusion tensor imaging tractography and constrained spherical deconvolution with automatic segmentation in traumatic brain injury. *NeuroImage Clin*. 2023;37:103284. [CrossRef]

20. Snider SB, Bodien YG, Frau-Pascual A, Bianciardi M, Foulkes AS, Edlow BL. Ascending arousal network connectivity during recovery from traumatic coma. *NeuroImage Clin*. 2020;28:102503. [CrossRef]

21. Snider SB, Bodien YG, Bianciardi M, Brown EN, Wu O, Edlow BL. Disruption of the ascending arousal network in acute traumatic disorders of consciousness. *Neurology*. 2019;93(13):e1281-e1287. [CrossRef]

22. Cuschieri S. The STROBE guidelines. *Saudi J Anaesth*. 2019;13(5)(suppl 1):S31-S34. [CrossRef]

23. Hoopes A, Mora JS, Dalca AV, Fischl B, Hoffmann M. SynthStrip: skull-stripping for any brain image. *Neuroimage*. 2022;260:119474. [CrossRef]

24. Bastin ME. Correction of eddy current-induced artefacts in diffusion tensor imaging using iterative cross-correlation. *Magn Reson Imaging*. 1999;17(7):1011-1024. [CrossRef]

25. Jenkinson M, Beckmann CF, Behrens TEJ, Woolrich MW, Smith SM. FSL. *Neuroimage*. 2012;62(2):782-790. [CrossRef]

26. Smith SM, Nichols TE. Threshold-free cluster enhancement: addressing problems of smoothing, threshold dependence and localisation in cluster inference. *Neuroimage*. 2009;44(1):83-98. [CrossRef]

27. Hua K, Zhang J, Wakana S, et al. Tract probability maps in stereotaxic spaces: analyses of white matter anatomy and tract-specific quantification. *Neuroimage*. 2008;39(1):336-347. [CrossRef]

28. Xiong K, Zhu Y, Zhang Y, et al. White matter integrity and cognition in mild traumatic brain injury following motor vehicle accident. *Brain Res*. 2014;1591(1):86-92. [CrossRef]

29. D'souza MM, Trivedi R, Singh K, et al. Traumatic brain injury and the post-concussion syndrome: a diffusion tensor tractography study. *Indian J Radiol Imaging*. 2015;25(4):404-414. [CrossRef]

30. Figley CR, Uddin MN, Wong K, Kornelsen J, Puig J, Figley TD. Potential pitfalls of using fractional anisotropy, axial diffusivity, and radial diffusivity as biomarkers of cerebral white matter microstructure. *Front Neurosci*. 2021;15:799576. [CrossRef]

31. Janve VA, Zu Z, Yao SY, et al. The radial diffusivity and magnetization transfer pool size ratio are sensitive markers for demyelination in a rat model of type III multiple sclerosis (MS) lesions. *Neuroimage*. 2013;74:298-305. [CrossRef]

32. Mahan MY, Rafter DJ, Truwit CL, Oswood M, Samadani U. Evaluation of diffusion measurements reveals radial diffusivity indicative of microstructural damage following acute, mild traumatic brain injury. *Magn Reson Imaging*. 2021;77:137-147. [CrossRef]

33. Veeramuthu V, Narayanan V, Kuo TL, et al. Diffusion tensor imaging parameters in mild traumatic brain injury and its correlation with early neuropsychological impairment: a longitudinal study. *J Neurotrauma*. 2015;32(19):1497-1509. [CrossRef]

34. Mac Donald CL, Dikranian K, Bayly P, Holtzman D, Brody D. Diffusion tensor imaging reliably detects experimental traumatic axonal injury and indicates approximate time of injury. *J Neurosci*. 2007;27(44):11869-11876. [CrossRef]

35. Timmers I, Roebroeck A, Bastiani M, Jansma B, Rubio-Gozalbo E, Zhang H. Assessing microstructural substrates of white matter abnormalities: a comparative study using DTI and NODDI. *PLoS One*. 2016;11(12):e0167884. [CrossRef]

36. Zhuo J, Raghavan P, Li J, et al. Longitudinal assessment of glymphatic changes following mild traumatic brain injury: insights from perivascular space burden and DTI-ALPS imaging. *Front Neurol*. 2024;15:1443496. [CrossRef]

37. Yeh FC, Irimia A, Bastos DCA, Golby AJ. Tractography methods and findings in brain tumors and traumatic brain injury. *Neuroimage*. 2021;245:118651. [CrossRef]

Effectiveness of Diffusion-Weighted Magnetic Resonance Imaging in Differentiating Mediastinal Lymphadenopathy

Türkhun Çetin[1], Fulya Memiş[2]

[1]Department of Radiology, Erzincan Binali Yıldırım University Faculty of Medicine, Erzincan, Türkiye
[2]Department of Internal Medicine, Erzincan Binali Yıldırım University Faculty of Medicine, Erzincan, Türkiye

Abstract

Objective: Several methods are used to diagnose mediastinal lymphadenopathy, which may result from many benign and malignant etiologies. Various radio-diagnostic imaging methods, bronchoscopy, mediastinoscopy, and thoracoscopy are used for diagnosis and management. This study attempted to enhance the diagnostic reliability of diffusion-weighted magnetic resonance imaging (MRI) for characterizing mediastinal lymph nodes and to identify conventional MRI sequences that could be beneficial.

Methods: A retrospective investigation was conducted on 40 patients exhibiting mediastinal lymphadenopathy as shown on chest MRI, including 27 with malignant and 13 with benign origins. The patients underwent echoplanar diffusion-weighted MRI, and apparent diffusion coefficient (ADC) maps were generated. The ADC values for lymph nodes located in the mediastinal region were computed. Additionally, statistical analysis was carried out, and the ADC values were connected to the findings of the histopathological examinations.

Results: The average assessment of the lymph nodes' ADC value that were malignant was found to be considerably lower ($P < .001$) compared to the value for lymph nodes that were benign. With a cut-off point of 1.50×10^{-3} mm²/s, the ADC variable is now being utilized. In the process of differentiating benign lymph nodes from malignant nodes, we were able to acquire a sensitivity rate of 85% and a specificity rate of 77%. The sensitivity and specificity values of short axis diameter measurements in this differentiation are 61% and 85%, respectively.

Conclusion: Apparent diffusion coefficient levels are essential in differentiating between benign and malignant mediastinal lymphadenopathies.

Keywords: ADC value, chest MRI, diffusion-weighted imaging, lymph node

INTRODUCTION

Mediastinal lymphadenopathy can result from diverse infectious (tuberculosis), inflammatory (sarcoidosis), and neoplastic (lung cancer, lymphoma, and extrathoracic cancer) diseases. The assessment of mediastinal lymphadenopathy is critical for efficient treatment and precise prognosis. Metastasis of lung cancer to mediastinal lymph nodes serves as a significant prognostic factor in staging.[1] Accurate diagnosis necessitates the integration of clinical, radiological, and pathological findings for effective management.[2]

The most effective approach in the staging of lymphadenopathy and differentiating between malignant and benign conditions in the mediastinum remains contentious. Diagnostic radiological imaging techniques, including computed tomography (CT) and magnetic resonance imaging (MRI), as well as invasive interventional procedures such as bronchoscopy, mediastinoscopy, and thoracoscopy, together with nuclear medicine imaging methods like positron emission tomography (PET), are employed in diagnosis.[1,3]

Computed tomography remains the primary imaging method for assessing thoracic abnormalities. The morphological characteristics, including the location, size, and distribution of lymph nodes, can be assessed via CT imaging. The evaluation of mediastinal lymph nodes via CT has historically relied on anatomical characteristics, particularly the measurement of the short diameter. Nonetheless, the sensitivity and specificity of this method have demonstrated low levels (nearly 60%).[4,5] F-18-deoxyglucose (FDG) uptake in lymph nodes during PET examinations is an alternative method for assessing lymphadenopathy that does not definitively confirm malignancy. Infectious or inflammatory lymphadenopathies show FDG uptake similar to malignant lymph nodes.[3-5] Surgical procedures like mediastinoscopy or thoracotomy are effective yet invasive and carry possible risks.[5]

Magnetic resonance imaging is another method employed to ascertain the existence and dimensions of lymph nodes. Standard MRI sequences are unable to differentiate between malignant and benign lymph nodes. Nonetheless, this distinction can be achieved through particular techniques, including diffusion-weighted imaging (DWI) and magnetization transfer imaging.[3-5] Besides differentiating between benign and malignant lymphadenopathy, MRI offers advantages over CT and PET, including superior soft tissue visualization and the absence of ionizing radiation.[6]

Diffusion-weighted imaging evaluates diffusion restrictions by detecting the microscopic Brownian movements of water within biological tissues, thereby reflecting the characteristics of those tissues. Measurement of the apparent diffusion coefficient (ADC) values allows for the achievement of a quantitative evaluation of the water molecule diffusion that occurs in these nodes.[7] Lymphadenopathies that are malignant have much lower ADC values as compared to lymph nodes that are benign.[8] This is the most effective non-invasive technique for distinguishing between benign and malignant mediastinal lymphadenopathy. It also provides the opportunity to initiate early treatment while awaiting the pathological diagnosis from invasive procedures.[8,9] Previously, numerous studies have shown the efficacy of DWI in the characterization of mediastinal lymphadenopathy.[1,3,4,8] Recently, Ramamoorthy et al[9] established that the ADC value is the paramount criterion for differentiating both benign and malignant mediastinal lymphadenopathies.

The purpose of this research was to enhance the diagnostic reliability of DWI for the characterization of mediastinal lymph nodes and to identify conventional MRI sequences that could be beneficial.

MATERIAL AND METHODS

This retrospective investigation obtained approval from the Erzincan University Ethics Committee (Number: 412235 2024-17/15 Date: December 16, 2024). All patients participating in the trial provided signed informed consent.

All imaging reports of contrast-enhanced chest MRI examinations conducted at our hospital's radiology clinic from January 2021 to November 2024 will be scanned utilizing the search term "mediastinal lymphadenopathy". Patients presenting with mediastinal lymphadenopathy will be evaluated by one of the authors, and those having diagnostic MR images, DWI sequences, and histopathological sampling of lymph nodes performed within a maximum of 1 month after MRI scanning and whose results are received from our hospital will be included in the study. Patients demonstrating motion artifacts in MR images, those for whom DWI images could not be obtained due to inadequate MR examinations stemming from factors such as claustrophobia, and individuals from whom histopathological sampling results were unachievable were excluded from the study.

The MRI scans were performed utilizing a 1.5 Tesla MRI device using a body phased-array coil (Siemens, Aera, Germany). During the entirety of the examination, patients were positioned in the supine posture. In order to acquire DW images, a single-shot echo-planar imaging sequence was utilized. These images were taken along the axial plane.

MAIN POINTS

- Computed tomography, magnetic resonance imaging (MRI), bronchoscopy, mediastinoscopy, thoracoscopy, and positron emission tomography are used for the evaluation and management of mediastinal lymphadenopathy.
- Magnetic resonance imaging, including diffusion-weighted sequences, serves as a non-invasive technique to ascertain the etiology of mediastinal lymphadenopathy.
- In addition to apparent diffusion coefficient measurement in mediastinal lymph nodes, evaluation of short-axis diameters and T2 heterogeneity increases diagnostic accuracy in characterization.

The DW MRI series encompassed the following parameters: on a scan that was triggered by respiration, every slice had a thickness of 6 millimeters. In the process of obtaining the DWI sequence, images with 2 different b values were obtained. These values were determined to be $b = 0b$ and $=400$ s/mm^2, respectively. Measurements and findings on DWI were performed on images with a b factor of 400 s/mm^2. The field of view was 360-400 mm, TR$=3800$ ms, TE$=70$ ms, and the matrix dimensions were 128×128. Images of ADC maps were generated automatically from each DW image, and quantitative measurements were carried out at workstations with the assistance of the Syngo® MR software system (Siemens, Germany).

A radiologist with 20 years of experience in thoracic radiology will then conduct a retrospective examination of the images without knowledge of the histopathological diagnosis or additional case details. The largest mediastinal lymph node will be identified in each patient. The localization, dimensions (particularly the short diameter), and appearance on standard MR sequences will be documented, and ADC values will be evaluated. The ADC values of these lymphadenopathies will be computed using the region-of-interest (ROI) placed. The width of the ROI circle will vary from 1 to 2 cm^2. The mean of 3 distinct ADC value measurements from the largest lymph node identified in each patient will be documented. The diameters of the short axis of the lymph nodes were also incorporated into the assessment. Furthermore, associated parenchymal lung pathologies depicted in the images will also be recorded. The contribution of ADC values and other MRI sequences to the diagnosis of benign or malignant lymphadenopathy will be evaluated by comparing the measured values with histopathological results.

Utilizing SPSS for Windows, version 24.0 (IBM SPSS Corp.; Armonk, NY, USA), the data were analyzed. The numerical parameters demonstrating a normal distribution that is normal were reported as mean ± standard deviation. The parameters that deviated from normal distribution of normality were reported as maximum and minimum values. The categorical parameters were presented as either numbers or percentages. The mean ADC values of the numeric variables across the diseased categories were analyzed using an ANOVA test with a 1-way design. The diagnostic performance of the testing method was assessed by receiver operating characteristic (ROC) curve analysis, shown by positive and negative predictive values, sensitivity, and specificity. In lymph nodes with a heterogeneous structure due to necrotic components, ROI placement was performed away from the necrotic area. The statistical significance of the results was determined by a P-value lower than .05.

RESULTS

Chest MRI scans of 52 patients with mediastinal lymphadenopathy reported within the specified time frame were analyzed. We excluded Four patients whose chest MR images were not sufficient for our evaluation and 8 patients who did not have histopathological sampling results of lymph nodes within 1 month after MRI at the hospital were excluded. Consequently, 40 patients who met the criteria were incorporated in the study. Twenty-six (65%) patients were male and the overall mean age was 55.4 ± 15.3 years.

Histopathological findings showed granulomatous diseases (tuberculosis and sarcoidosis) in 10 patients, metastatic bronchogenic carcinoma in 8 patients, non-Hodgkin lymphoma in 7 patients, Hodgkin lymphoma in 6 patients, metastatic lymph nodes from distant regions in 6 patients, and reactive lymphoid hyperplasia in 3 patients. The mean ADC values measured according to these pathologies are shown in Table 1.

Table 1. Mean ADC Values of Mediastinal Lymphadenopathy

Histopathological Diagnosis	n	Mean ± SD ($\times10^{-3}$ mm²/s)
Granulomatous diseases		
Tuberculosis	4	1.94 ± 0.44
Sarcoidosis	6	1.78 ± 0.35
Metastatic bronchogenic carcinoma		
SCLC	3	1.19 ± 0.27
NSCLC	5	1.35 ± 0.15
Non-Hodgkin lymphoma	7	0.89 ± 0.23
Hodgkin lymphoma	6	0.95 ± 0.13
Metastatic lymph nodes from distant		
Breast cancer	3	0.99 ± 0.28
Thyroid carcinoma	1	1.08
Esophageal cancer	1	0.95
Renal cell carcinoma	1	1.11
Reactive lymphoid hyperplasia	3	2.10 ± 0.46

There were 13 patients presented with benign conditions, yielding a mean ADC value, as determined by the largest lymph nodes that are the largest at $1.90 \pm 0.45 \times 10^{-3}$ mm²/s. Conversely, the average ADC value of lymphadenopathies in 27 individuals with malignancy was $1.05 \pm$ 0.25×10^{-3} mm²/s. Comparative analysis of these data revealed that the assessed ADC levels effectively distinguished between benign and malignant lymphadenopathies ($P < .001$). Our attempts to differentiate between malignant lymph nodes based on their etiology, such as lymphoma or metastasis, using ADC measurements yielded no significant results.

Non-Hodgkin's lymphoma exhibited the lowest mean ADC values, whereas granulomatous lymphadenopathy resulting from tuberculosis demonstrated the highest mean ADC values.

In the ROC analysis, utilizing a threshold of 1.50×10^{-3} mm²/s for the ADC variable, we observed a sensitivity of 85%, a specificity of 77%, a positive predictive value of 78.7%, and a negative predictive value of 83.7% in differentiating benign from malignant lymph nodes.

The mean short-axis diameter of lymph nodes was 2.86 ± 1.02 cm (range: 0.7-7.5 cm). All of the subcentimetric ones belonged to reactive lymph nodes. The mean short-axis diameter of the lymph nodes in the benign group was 1.71 ± 0.55 cm. In the malignant group, the average short-axis diameter was 3.41 ± 0.98 cm. Benign and malignant lesions could be differentiated based on short-axis diameter ($P = .03$). The evaluation
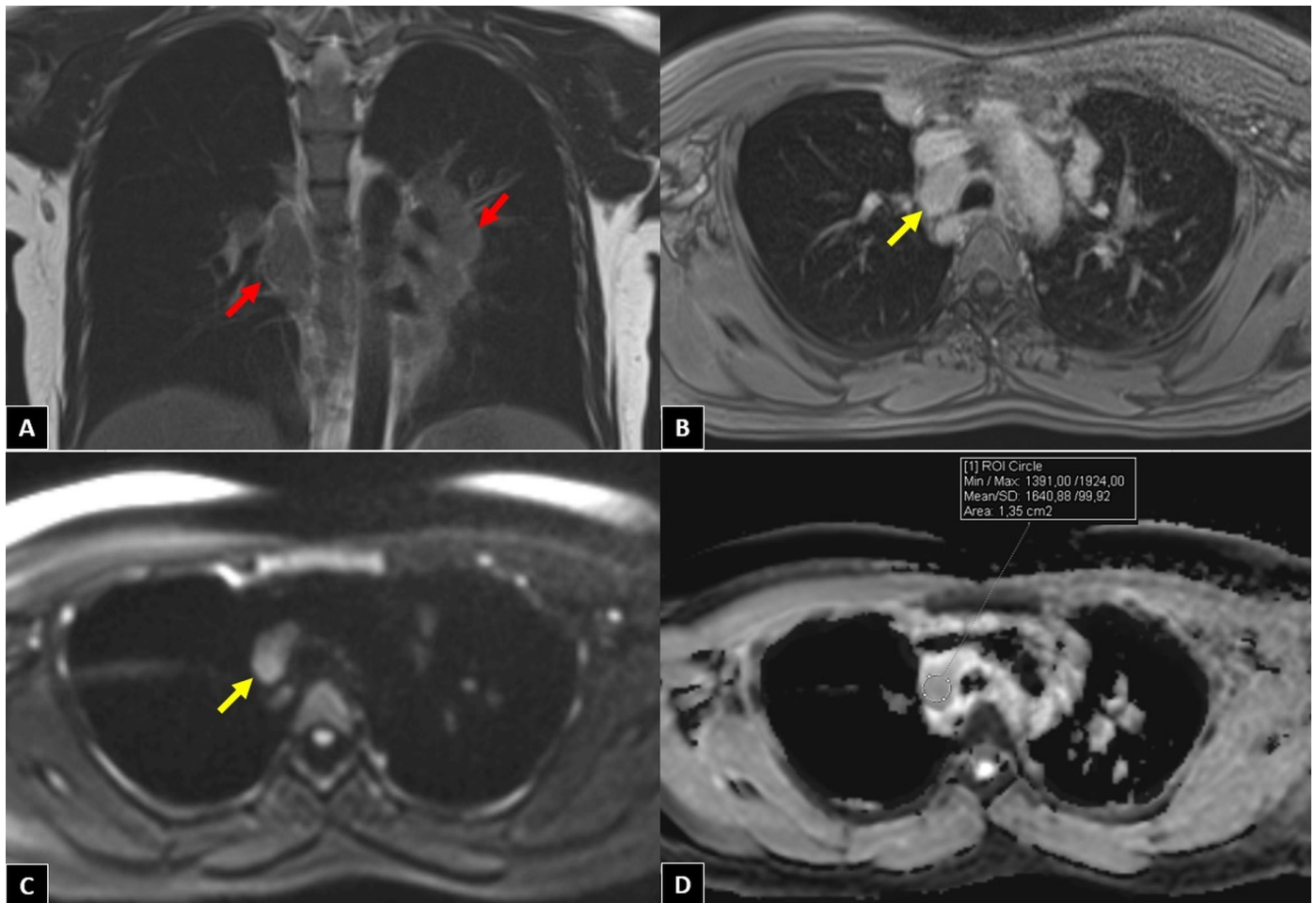
Figure 1. A 38-year-old patient with sarcoidosis. (A) Coronal T2W magnetic resonance (MR) image shows multiple bilateral hilar lymphadenopathy (red arrows); (B) axial post-contrast T1W MR image shows hyper-enhancing right upper paratracheal lymph node (yellow arrow); (C) b=800 s/mm² diffusion-weighted MR image shows hyperintense right upper paratracheal lymph node (yellow arrow); (D) in the ADC map image, the mean ADC value of this lymph node was measured as 1.64×10^{-3} mm²/s.
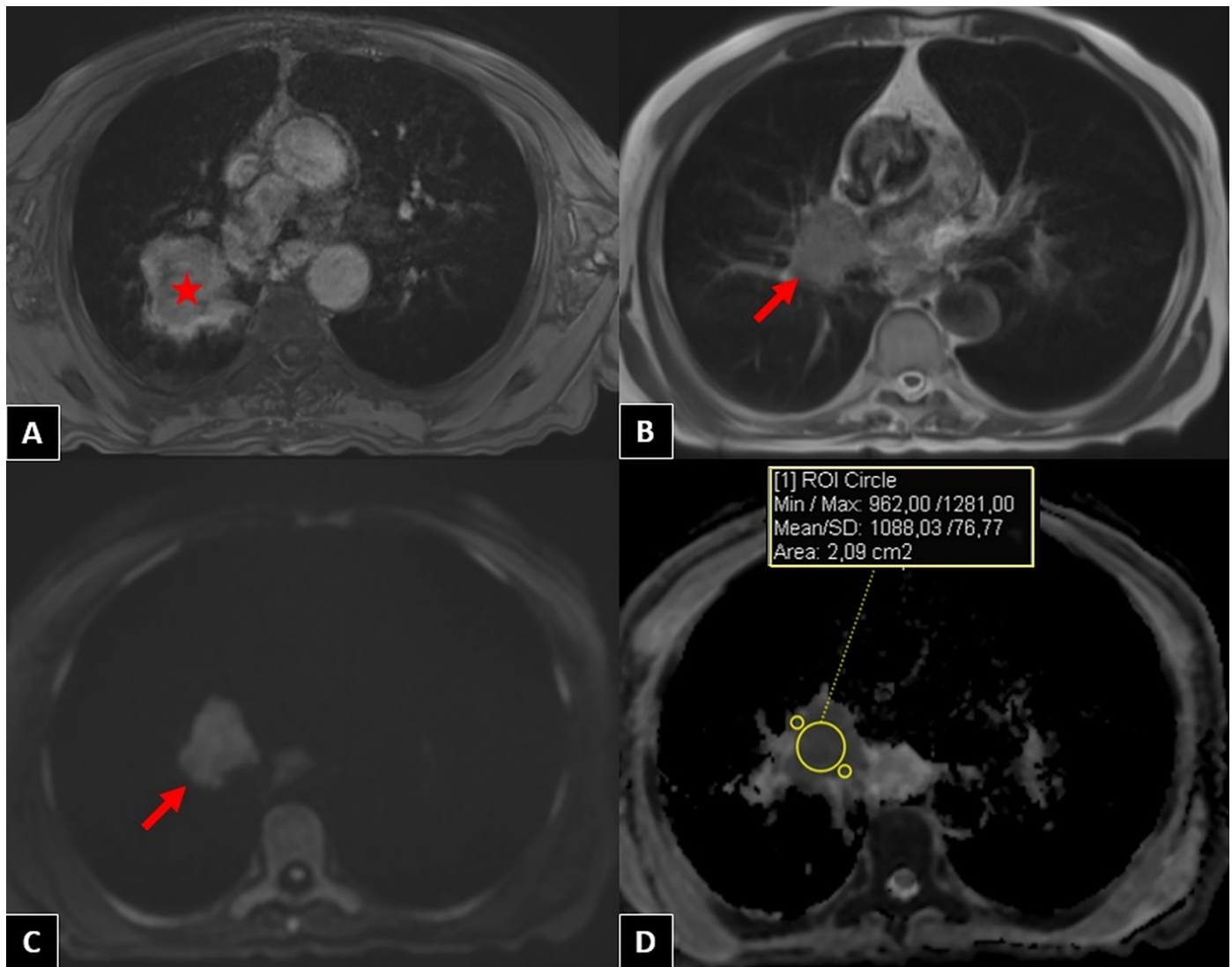
Figure 2. A 65-year-old patient with non-small cell lung cancer. (A) An axial post-contrast T1W magnetic resonance (MR) image shows a hyper-enhancing right upper lobe lung mass (red asterisk); (B) an axial T2W MR image shows right hilar lymphadenopathy (red arrow); (C) A b=800 s/mm² diffusion-weighted MR image shows hyperintense right hilar lymphadenopathy (red arrow); (D) in the ADC map image, the mean ADC value of this lymph node was measured as 1.08× 10^{-3} mm²/s.

of lymphadenopathies based on short-axis diameters for the purpose of distinguishing between benign and malignant lymphadenopathies showed a sensitivity of 61% and a specificity of 85%, respectively.

The signal intensities of lymph nodes assessed in T1 and T2-weighted conventional MR sequences exhibited no significant difference between benign and malignant groups.

Figures 1 and 2 show chest MRI images of patients with sarcoidosis and non-small cell lung cancer (NSCLC), respectively.

DISCUSSION
Different methods are employed in diagnosing mediastinal lymphadenopathy, which may arise from numerous benign and malignant etiologies. Computed tomography is primarily utilized for the identification of mediastinal lymphadenopathy, with only morphological characteristics being recognized. The gold standard for definitive diagnosis is histopathological sampling via mediastinoscopy, an invasive procedure.

Recent studies utilizing ADC measurements in MRI have produced encouraging outcomes in lesion characterization.[3-6]

In the present study, the mean ADC measurement for malignant lymph nodes was substantially reduced ($P < .001$) compared to the values for benign lymph nodes. The primary cause is believed to be the hypercellularity of malignant lesions. Hypercellularity reduces the diffusion area of extracellular water molecules, resulting in lower ADC values in malignant lesions.[10]

Compared to histopathology results, the measurement of ADC values has 85% sensitivity and 77% specificity for the characterization of mediastinal lymphadenopathy (benign and malignant). Wu et al[11] conducted a meta-analysis in which they compared the lymphadenopathies of patients with NSCLC with the lymph nodes of healthy persons. They found that the pooled sensitivity for DWI parameters was assessed to be 72%, while the specificity was around 95%. In comparison to our investigation, the specificity in this meta-analysis was greater;

nevertheless, our approach has shown higher sensitivity. Increased sensitivity is a significant parameter in cancer diagnosis.

In our investigation, we determined 1.50×10^{-3} mm²/s as the ideal cutoff ADC threshold for distinguishing benign from malignant lymph nodes according to the ROC curve. Different results have been obtained using different threshold values in the literature. Diverse results have been produced with varying threshold ADC values in the literature. Sigovan et al[1] found sensitivity 68.2% and specificity of 84.6% for benign and malignant lymph node differentiation with a cutoff ADC value of 1.28×10^{-3} mm²/s. In another study, Abdel Razek et al[4] reported sensitivity and specificity rates of 96.4% and 71.4%, respectively, for differentiating between benign and malignant lymph nodes, using a cutoff ADC value of 1.85×10^{-3} mm²/s. These results show that an increase in the ADC value used as a threshold for mediastinal lymph node characterization enhances sensitivity while diminishing specificity. This factor must be considered while establishing the threshold value.

The ADC value of metastatic lymphadenopathies was higher than that of lymphoma in our analysis; however, this difference was not statistically significant. Moreover, this present research observed no substantial variation in ADC values for lymphadenopathy between Hodgkin and non-Hodgkin lymphoma, although Sabri et al[12] found notable differences in ADC values for both lymphoma types in a prior study. Research findings utilizing diffusion MRI and ADC measures for textural analysis of mediastinal lymphadenopathy indicate that ADC values are the most significant parameter for identifying lymph nodes affected by lymphoma.[13] These studies highlighted that lymphoma exhibited the lowest mean ADC value among malignant pathologies. The primary benefit of this circumstance in clinical practice is significant at this juncture. Lymphoma involvement can be identified if a specific threshold value is established by assessing tiny lymph nodes, which are challenging to diagnose, by ADC measurement.

Despite the lack of significant findings in our study, existing literature demonstrates that the heterogeneity shown in T2-weighted MRI images is much more prevalent in malignant lymph nodes.[9,14] Ramamoorthy et al[9] reported that T2 heterogeneity has a sensitivity of 72.2% and a specificity of 84% in distinguishing malignancies from benign lymph nodes in the mediastinum. According to these results, T2 heterogeneity provides lymph node characterization with a precision close to ADC measurement.

It has been shown in the research, along with several studies in the literature, that short-axis diameter assessment may effectively distinguish between benign and malignant lymphadenopathies. Although it is not as high as ADC measurement, its sensitivity and specificity are promising.[2,4,9] Based on these findings, we may enhance diagnostic sensitivity and specificity by combining T2 heterogeneity and short-axis diameter measurements with ADC data.

The diffusion MRI images acquired from all patients in the investigation were obtained prior to the administration of various therapies. Recent literature indicates that the monitoring of ADC values has been effective in assessing treatment response, particularly in malignant lymph nodes. Besides alterations in lymphadenopathy size, diffusion MRI and ADC values can provide insights into the cellular composition of the lymph node. Usuda et al[15] demonstrated that diffusion MRI outperformed CT in assessing the treatment response of malignant lymph nodes. The absence of post-treatment imaging data constitutes an important constraint in our research.

This research has a few limitations to consider. First of all, since a retrospective single-center study was conducted, the generalizability of the results is weak. The sample size is fairly limited, and the incidence of patients with lymphadenopathy due to benign causes is notably low. This may impact the efficacy and reliability of statistical analyses. Further study involving larger cohorts is essential for strengthening the statistical significance of these results. When it comes to the differential diagnosis of mediastinal lymphadenopathies, the combination of ADC values with biological markers that have the potential to affect the accuracy of diagnosis has not been carried out.

Apparent diffusion coefficient levels are useful in distinguishing benign and malignant mediastinal lymphadenopathies. Consequently, unnecessary utilization of mediastinoscopy, an invasive diagnostic procedure, may be spared.

REFERENCES
1. Sigovan M, Akl P, Mesmann C, et al. Benign and malignant enlarged chest nodes staging by diffusion-weighted MRI: an alternative to mediastinoscopy? *Br J Radiol*. 2018;91(1082):20160919. [CrossRef]
2. Iyer H, Anand A, Sryma PB, et al. Mediastinal lymphadenopathy: a practical approach. *Expert Rev Respir Med*. 2021;15(10):1317-1334. [CrossRef]
3. Koşucu P, Tekinbaş C, Erol M, et al. Mediastinal lymph nodes: assessment with diffusion-weighted MR imaging. *J Magn Reson Imaging*. 2009;30(2):292-297. [CrossRef]
4. Abdel Razek AA, Elkammary S, Elmorsy AS, Elshafey M, Elhadedy T. Characterization of mediastinal lymphadenopathy with diffusion-weighted imaging. *Magn Reson Imaging*. 2011;29(2):167-172. [CrossRef]
5. Santos FS, Verma N, Marchiori E, et al. MRI-based differentiation between lymphoma and sarcoidosis in mediastinal lymph nodes. *J Bras Pneumol*. 2021;47(2):e20200055. [CrossRef]
6. Cinar HG, Memis KB, Oztepe MF, Fatihoglu E, Aydin S, Kantarci M. Effectiveness of apparent diffusion coefficient values in predicting pathologic subtypes and grade in non-small-cell lung cancer. *Diagnostics (Basel)*. 2024;14(16):1795. [CrossRef]
7. Li G, Huang R, Zhu M, et al. Native T1-mapping and diffusion-weighted imaging (DWI) can be used to identify lung cancer pathological types and their correlation with Ki-67 expression. *J Thorac Dis*. 2022;14(2):443-454. [CrossRef]
8. Abou Youssef HA, Elzorkany MA, Hussein SA, Taymour TA, Abdel Gawad MH. Evaluation of mediastinal lymphadenopathy by diffusion weighted MRI; correlation with histopathological results. *Adv Respir Med*. 2019;87(3):175-183. [CrossRef]
9. Ramamoorthy E, Garg M, Singh P, Aggarwal AN, Gupta N. Role of diffusion-weighted magnetic resonance imaging for characterization of mediastinal lymphadenopathy. *Diagnostics (Basel)*. 2023;13(4):706. [CrossRef]

10. Koh DM, Collins DJ. Diffusion-weighted MRI in the body: applications and challenges in oncology. *AJR Am J Roentgenol*. 2007;188(6):1622-1635. [CrossRef]

11. Wu LM, Xu JR, Gu HY, et al. Preoperative mediastinal and hilar nodal staging with diffusion-weighted magnetic resonance imaging and fluoro-deoxyglucose positron emission tomography/computed tomography in patients with non-small-cell lung cancer: which is better? *J Surg Res*. 2012;178(1):304-314. [CrossRef]

12. Sabri YY, Ewis NM, Zawam HEH, Khairy MA. Role of diffusion MRI in diagnosis of mediastinal lymphoma: initial assessment and response to therapy. *Egypt J Radiol Nucl Med*. 2021;52(1):215. [CrossRef]

13. De Paepe KN, De Keyzer F, Wolter P, et al. Improving lymph node characterization in staging malignant lymphoma using first-order ADC texture analysis from whole-body diffusion-weighted MRI. *J Magn Reson Imaging*. 2018;48(4):897-906. [CrossRef]

14. de Bondt RBJ, Hoeberigs MC, Nelemans PJ, et al. Diagnostic accuracy and additional value of diffusion-weighted imaging for discrimination of malignant cervical lymph nodes in head and neck squamous cell carcinoma. *Neuroradiology*. 2009;51(3):183-192. [CrossRef]

15. Usuda K, Iwai S, Funasaki A, et al. Diffusion-weighted magnetic resonance imaging is useful for the response evaluation of chemotherapy and/or radiotherapy to recurrent lesions of lung cancer. *Transl Oncol*. 2019;12(5):699-704. [CrossRef]

Branch-to-Total Pulmonary Artery Area Ratio as a Predictor of Flow Limitation in Tetralogy of Fallot: MRA and Phase Contrast MRI Study

Ali Fuat Tekin[1] , Tuba Banaz[1] , Ömer Altun[1] , Berk Tütüncüoğlu[1] , Muhammed Faruk Kazanbaş[1] , Mehmet Kadıoğlu[1] , Mustafa Kan[1] , Yiğit Can Kartal[1] , İlker Kemal Yücel[2] , Serçin Özkök[1]

[1]Department of Radiology, Başakşehir Çam and Sakura City Hospital, İstanbul, Türkiye
[2]Department of Pediatric Cardiology, İstanbul University-Cerrahpaşa Faculty of Medicine, İstanbul, Türkiye

Abstract

Objective: The severity of branch pulmonary artery stenosis and associated flow restriction can be assessed using catheter angiography and lung perfusion scintigraphy. However, these techniques are time-consuming and have various limitations. This study aims to establish a ratio of the narrowed-to-total pulmonary artery area to assess flow restriction.

Methods: A net flow of the right and left pulmonary arteries was calculated by phase-contrast magnetic resonance imaging (MRI), and the cross-sectional area was calculated at the narrowest point of the branch pulmonary artery using multiplanar reconstruction images from magnetic resonance angiography. A right-to-left pulmonary artery flow ratio between 61/39 and 43/57 was considered normal. The narrowed-to-total pulmonary artery area ratio was calculated to establish a threshold for physiologically significant branch pulmonary artery stenosis.

Results: A total of 272 patients were included in the study. About 136 patients diagnosed with branch pulmonary artery stenosis were compared with 136 patients exhibiting normal branch pulmonary artery flow. The patients with branch pulmonary artery stenosis exhibited a significantly reduced narrowed-to-total pulmonary artery area ratio, with values of 0.46 and 0.38, respectively, showing a statistically significant difference (P < .00001). A branch-to-total pulmonary artery area ratio of ≤0.40 exhibited a sensitivity of 67.65% and a specificity of 91.91% in detecting branch pulmonary artery stenosis, as confirmed by the calculated area under the curve of 0.86 with a 95% CI ranging from 0.813 to 0.899 (P < .0001). The positive predictive value was 84.79%, and the negative predictive value was 80.99%.

Conclusion: A narrowed-to-total pulmonary artery area ratio of ≤0.40, measured by cross-sectional imaging, can help identify patients who may need catheter angiography, especially when cardiac MRI is unavailable or flow measurement is not possible.

Keywords: Cardiac magnetic resonance imaging, magnetic resonance angiography, phase contrast imaging, pulmonary artery stenosis, tetralogy of Fallot

INTRODUCTION

Tetralogy of Fallot is the most common cyanotic congenital heart disease and usually requires surgical correction during the first years of life.[1] Branch pulmonary artery stenosis, which is one of the most common complications, occurs in 20%-40% of patients after surgical repair, either due to the primary nature of the disease or secondary to surgical interventions.[2]

Evaluating the severity of branch pulmonary artery stenosis following surgical correction is crucial, as branch pulmonary artery stenosis not only exacerbates pulmonary insufficiency but also serves as a key predictor of outcomes and exercise capacity.[3,4]

The current standard care for patients with branch pulmonary artery stenosis involves a series of time-consuming diagnostic procedures, which include catheter angiography and Tc-99-labeled macro-aggregated albumin perfusion scintigraphy. However, both conventional catheter angiography and lung scintigraphy have some limitations in evaluating branch pulmonary artery stenosis. Conventional catheter angiography is not able to assess preferential pulmonary blood flow, while Tc-99 scintigraphy may produce false-negative results in bilateral stenosis or false-positive findings in cases of multi-vessel distal obstructions, parenchymal diseases, or aortopulmonary collaterals.[5]

The anatomic evaluation of the pulmonary artery by echocardiography, computed tomography, and magnetic resonance angiography remains a widely used method for determining the hemodynamic significance of stenoses and assessing the need for angioplasty or stenting.[6-8] However, it was demonstrated that the branch pulmonary artery diameter ratios fail to predict flow discrepancies.[9]

On the other hand, phase-contrast magnetic resonance imaging (MRI) offers a reliable, non-invasive alternative for evaluating branch pulmonary artery stenosis and flow characteristics without ionizing radiation or radionuclides.[10-14] However, long examination time, the requirement for anesthesia, high cost, and the need for trained personnel are the most important limitations to its widespread use. Therefore, this study aims to establish a ratio of the narrowed to the total pulmonary artery cross-sectional area derived from magnetic resonance angiography (MRA) for branch pulmonary artery stenosis that indicates blood flow restriction, using phase-contrast MRI in children following Tetralogy of Fallot repair.

METHODS
Ethics Committee of İstanbul Medeniyet University (Date 25.12.2019, Approval Number: 2019/052) approved this retrospective, single-center study, and the requirement for informed consent was waived.

Study Population
A total of 532 patients who underwent a cardiac MRI with phase contrast MRI and MRA between January 2015 and July 2020 were retrospectively analyzed. Magnetic resonance imaging examinations with poor image quality were excluded. In patients with multiple studies, the most recent eligible examination was used. Patients with right ventricle-to-pulmonary artery conduit, left-to-right shunt, major aortopulmonary collaterals, or those who had pulmonary artery interventions (stenting, balloon dilatation, or pulmonary valve replacement) were excluded.

The patients who had total surgical correction with a native right ventricular outflow tract and a branch pulmonary artery higher than 20 mmHg were accepted as the branch pulmonary artery stenosis group.

Patients with no branch pulmonary artery stenosis, with a Doppler gradient lower than 20 mmHg reported within 6 months before the MRI examination, were accepted as a control group.

The demographic data and the surgical information for these patients were obtained from the national health information system. The inclusion and exclusion criteria of the study are presented in the flowchart (Figure 1).

Magnetic Resonance Imaging Protocol and Evaluation
All cardiovascular MRI examinations were conducted using a 1.5-Tesla scanner (Signa HDx; GE Medical Systems, Milwaukee, WI, USA, and Siemens Avanto, Erlangen, Germany) equipped with a 32-channel phased-array abdominal coil and electrocardiographic gating. Intravenous sedation was not administered during the examination. The

---

MAIN POINTS

- Accurately detecting significant branch pulmonary artery stenosis in cross-sectional imaging remains challenging when flow assessment by phase-contrast magnetic resonance imaging is unavailable, delaying appropriate intervention.
- A narrowed-to-total pulmonary artery area ratio of ≤ 0.40 reliably distinguished significant stenosis, with almost 68% sensitivity and 92% specificity.
- Measuring the narrowed-to-total pulmonary artery area ratio on cross-sectional imaging provides a rapid, noninvasive tool to identify clinically relevant stenosis, guiding timely referral for intervention and potentially improving patient outcomes.

---

images were acquired during 1 or 2 breath-holds of 8-12 seconds duration, depending on the heart rate during the end-expiratory breath-hold. The duration of the examination varied between 15 and 30 minutes.

The examinations and evaluations were conducted by a radiologist with at least 10 years of experience in congenital cardiac imaging. A 3-plane localizer was initially obtained through the thorax using a steady-state free precession sequence. Subsequently, cine steady-state free precession sequences were acquired for 2-chamber, 4-chamber, and short-axis views for all patients.

Time-resolved contrast-enhanced MRAs were obtained using a gradient echo inversion recovery sequence with Electrocardiography (ECG) gating following injection of a gadolinium-based contrast at a dose of 0.2 mmol/kg. The imaging parameters of the MRA included TR: 4.0-4.4 ms; TE: 2.2-2.3 ms; flip angle: 15°; receiver bandwidth: 31.25 kHz; field-of-view: 360-440 × 360-440 mm²; acquisition voxel size: 2 × 2 × 2-2.2 × 2.2 × 2.2 mm³; number of excitations: 4, hyperkat acceleration = 6-8× and temporal resolution 31-63 milliseconds.

Phase contrast MRI was performed for flow measurements through the right and left branch pulmonary arteries. Each image set was obtained with retrospective gating and comprised 25 reconstructed cardiac phases according to the heart rate. The optimal velocity encoding value for the pulmonary artery was calculated using the Bernoulli equation based on the gradients reported in the echocardiography report. The phase contrast MRI was performed with retrospective ECG gating and the following imaging parameters: TR/TE, 25/6 milliseconds; slice thickness, 6 mm; flip angle, 30°; receiver bandwidth, 31.25 kHz; rectangular field of view, 260 to 400 mm; matrix, 256 × 256; and number of excitations, 2. The phase contrast MRI of the right and the left pulmonary arteries is prescribed at the midpoint perpendicular to the vessels by the double-oblique technique. The slice location was determined by the reconstructed multiplanar images of MRA. To decrease the turbulent artifact, the imaging planes were located distal to the stenotic area if present.

The subjects' weights and height were recorded to calculate the body surface area, and all measurements were indexed.

Branch Pulmonary Artery Magnetic Resonance Imaging/ Magnetic Resonance Angiography Measurements
Multiplanar reconstructions of the MRA on the pulmonary artery phase were used to measure branch pulmonary artery cross-sectional areas in 2 orthogonal dimensions at the narrowest point on a dedicated workstation. The pulmonary artery phase of the MRA was used for measurements. The cross-sectional diameter of the branch pulmonary artery was determined at its narrowest point using multiplanar reconstruction images derived from MRA. The longest and the shortest diameters of the vessel were measured and recorded for both pulmonary arteries from the inner-to-inner contour of the vessel. The formula for calculating the cross-sectional area of the branch pulmonary artery is provided below. This formulation is derived based on the area calculation of the ellipse.

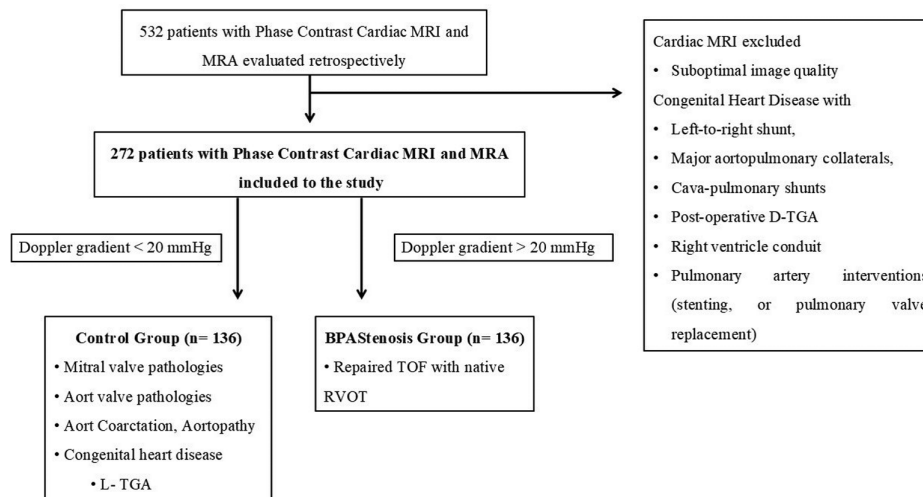$$\text{Area} = [\pi \times R_S \times R_L] / 4$$

R_S = minor radius,

R_L = major radius,

$\pi \sim 3.14$

Figure 1. Flow chart showing the patient selection with inclusion and exclusion criteria. BPA, branch pulmonary artery; LPA, left pulmonary artery; MRA, magnetic resonance angiography; MRI, magnetic resonance imaging; RPA, right pulmonary artery; RVOT, right ventricular outflow tract; TGA, transposition of great arteries; Tetralogy of Fallot, transposition of great arteries.

For the flow analysis of the branch pulmonary arteries, the contours of the left and right pulmonary arteries were automatically contoured and manually corrected, propagated through all cardiac phases. The distribution of blood flow between the right and left pulmonary arteries was calculated as the net right pulmonary artery flow volume divided by the total net flow volume of both pulmonary arteries, expressed as a percentage. A right-to-left pulmonary artery flow ratio was calculated, with a range of 61:39 to 43:57 considered physiologically normal, based on established literature values.[14] The measurement and the calculation are represented in Figures 2 and 3 for the patients in the control and branch pulmonary artery stenosis groups. The patients were divided into 6 groups according to age: Group 1, 1-8 years; Group 2, 8-18 years; Group 3, 19-30 years; Group 4, 30+ years. All the measurements and evaluations were performed using dedicated software (Philips IntelliSpace V 11.0, Philips Medical Imaging Systems, Leiden, the Netherlands).

Statistical Analysis

The obtained data were analyzed using SPSS version 20.0 software (IBM Corporation, Armonk, NY, USA). The median values (interquartile range, 25th–75th percentiles) were used to present the descriptive values. Differences between patient groups were evaluated with nonparametric paired tests to account for data matching (Kruskal–Wallis and Mann–Whitney U test). Pearson correlation coefficients were used to assess the correlation of the narrowed-to-total pulmonary artery area ratio with age and gender. Simple linear regression on each set of measurements was used to generate prediction equations relating to the narrowed-to-total pulmonary artery area ratio; goodness of fit was assessed with R^2. A narrowed-to-total branch pulmonary artery area ratio with a discriminatory value suggestive of unilateral branch pulmonary artery stenosis and its receiver operating characteristic (ROC) area under the curve was calculated. A P-value of less than .05 was considered significant.

RESULTS

In this retrospective study, 272 patients with a male-to-female ratio of 1.6:1 (105 female and 167 males) were included. The median age was 16 years (11-21). One hundred thirty-six patients (F/M= 83/53)

exhibiting normal branch pulmonary artery flow, who served as the control group, with a mean age of 15.5 years (12-22), were included in the study, alongside 136 patients (F/M= 84/52) diagnosed with branch pulmonary artery stenosis, with a mean age of 16 years (11-20), for comparison.

The diameter of the right pulmonary artery and left pulmonary artery was 17 mm (2-20) and 15 mm (5-15) in the control group vs. 15 mm (5-18) and 12.5 mm (5-16) in the branch pulmonary artery stenosis group. The cross-sectional area of the right pulmonary artery and left pulmonary artery was 209.5 mm^2 (73-314) and 176 mm^2 (73-296) in the control group vs. 164 mm^2 (64-314) and 113 mm^2 (52-225) in the branch pulmonary artery stenosis group.

There was a statistically significant difference between control and branch pulmonary artery stenosis groups regarding left pulmonary artery diameter, cross-sectional area, and z-score ($P = .006$, $P = .002$, and $P < .00001$, respectively). However, no statistically significant difference was found in terms of right pulmonary artery diameter, cross-sectional area, and z-score ($P = .522$, $P = .495$, and $P = .317$, respectively). No statistical difference was found for gender in terms of the cross-sectional area of the right pulmonary artery and left pulmonary artery ($P = .697$ and $P = .741$, respectively) in the control group and branch pulmonary artery stenosis group ($P = .810$ and $P = .471$, respectively). Demographic findings and the details of the measurements are presented in Table 1.

The narrowed-to-total pulmonary artery area ratio was 0.46 vs. 0.38 in the control group and patients with branch pulmonary artery stenosis. There was a statistically significant difference between the control and branch pulmonary artery stenosis group regarding the narrowed-to-total pulmonary artery area ratio ($P < .00001$). No statistical difference was found between genders in the control group of patients with branch pulmonary artery stenosis (0.44 in boys and 0.43 in girls, $P = .968$) and (0.37 in boys and 0.36 in girls, $P = .794$). The difference in the narrowed-to-total pulmonary artery area ratio between control and branch pulmonary artery stenosis groups was statistically significant across all age groups (Table 2).
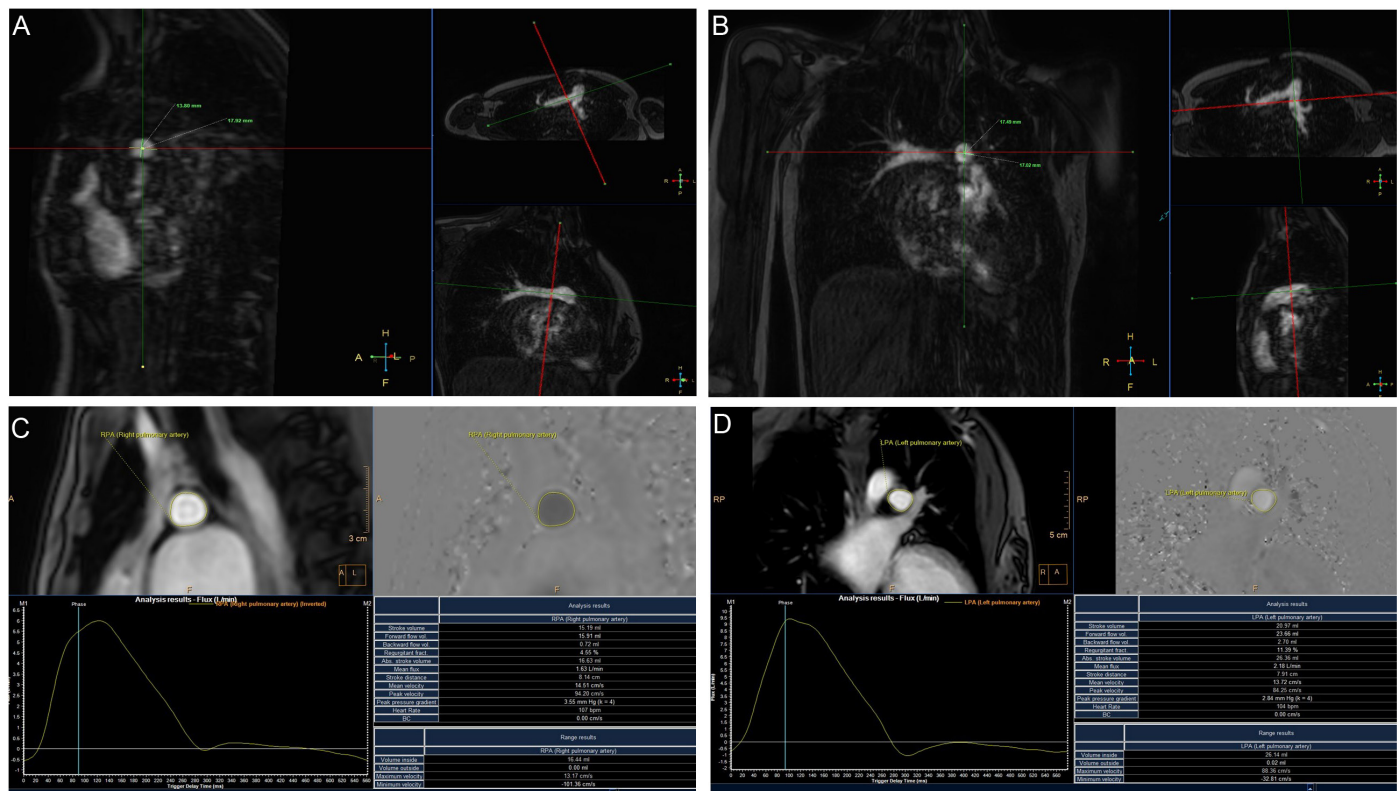
Figure 2. (A-D) A 19-year-old female in the control group. Measurement of the right pulmonary artery (A) and left pulmonary artery (B) in multiplanar reconstructed images of MRA. Phase contrast MRI measurement for the right pulmonary artery (C) and left pulmonary artery (D). The area for the right and left pulmonary arteries are calculated as 194 mm^2 ((3.14 × 13.8 × 17.9)/4) and 234 mm^2 ((3.14 × 17.5 × 17)/4), respectively. The narrowed-to-total pulmonary artery area ratio is calculated as 0.45 (194/428). Net right and left pulmonary artery flows are measured as 15 mL and 21 mL, respectively. The right-to-left pulmonary artery flow ratio is calculated as 42/58%, which is accepted within the normal range.

In the branch pulmonary artery stenosis group, no statistical difference was found in terms of the narrowed-to-total pulmonary artery area ratio between the 4 groups ($P=.055$). Also, no statistical difference was found between patients younger (0.39, 0.33-0.43) and older (0.37, 0.30-0.41) than 18 years old ($P = .173$).

The linear regression analysis revealed the following equation: Y = 0.3929 + −0.001475x. The model's R^2 value was 0.02799 and $P=.0516$, suggesting that age has a minimal but non-significant effect on the ratio.

A ratio of ≤0.40 exhibited a sensitivity of 67.65% and a specificity of 91.91% in detecting branch pulmonary artery stenosis, as confirmed by the calculated area under the curve (AUC) of 0.86 with a 95% CI ranging from 0.813 to 0.899 and a P-value of <.0001. The estimated positive predictive value (PPV) was 84.79%, and the negative predictive value (NPV) was 80.99 % (Figure 3, 4).

DISCUSSION
This study demonstrated the narrowed-to-total pulmonary artery area ratio as a novel indicator for assessing flow restriction in patients with branch pulmonary artery stenosis. For the first time, this ratio was shown to effectively discriminate patients with clinically significant branch pulmonary artery stenosis without additional diagnostic techniques. A threshold value of 0.4 was identified, enabling the differentiation of patients with physiologically significant stenosis from those without. This finding highlights the potential of this ratio as a simple

and non-invasive metric for clinical decision-making in evaluating branch pulmonary artery stenosis.

Different imaging modalities, such as Doppler echocardiography, catheter angiography, or MRI/MRA, have been used to diagnose branch pulmonary artery stenosis. While catheter angiography is considered the gold-standard imaging technique for evaluating anatomical and gradient changes in branch pulmonary artery stenosis and guides the treatment (balloon dilation, stenting) to improve pulmonary blood flow, it carries various limitations, such as exposure to ionizing radiation, the need for iodinated contrast agents, and the inability to quantify flow and cardiac function effectively.[5,15]

Tc-99m-labeled macro-aggregated albumin perfusion scintigraphy is accepted as a gold-standard non-invasive imaging method for assessing lung perfusion.[5,16] However, it is prone to false-negative results in cases of bilateral BPA stenosis or false-positive findings in patients with multi-vessel distal stenosis, parenchymal diseases, or aortopulmonary collaterals.[17,18] Additionally, in patients with cavopulmonary connections, preferential drainage of caval blood into the right or left pulmonary artery can limit the accuracy of this technique.[19] In recent years, phase-contrast MRI has emerged as an effective alternative to radiation-containing perfusion scintigraphy for precisely quantifying differential pulmonary blood flow.[10] As reported by Fratz et al[19], phase-contrast MRI has been shown to provide more accurate evaluations of pulmonary perfusion ratios compared to lung perfusion scintigraphy, particularly in patients with congenital heart disease, such as those with
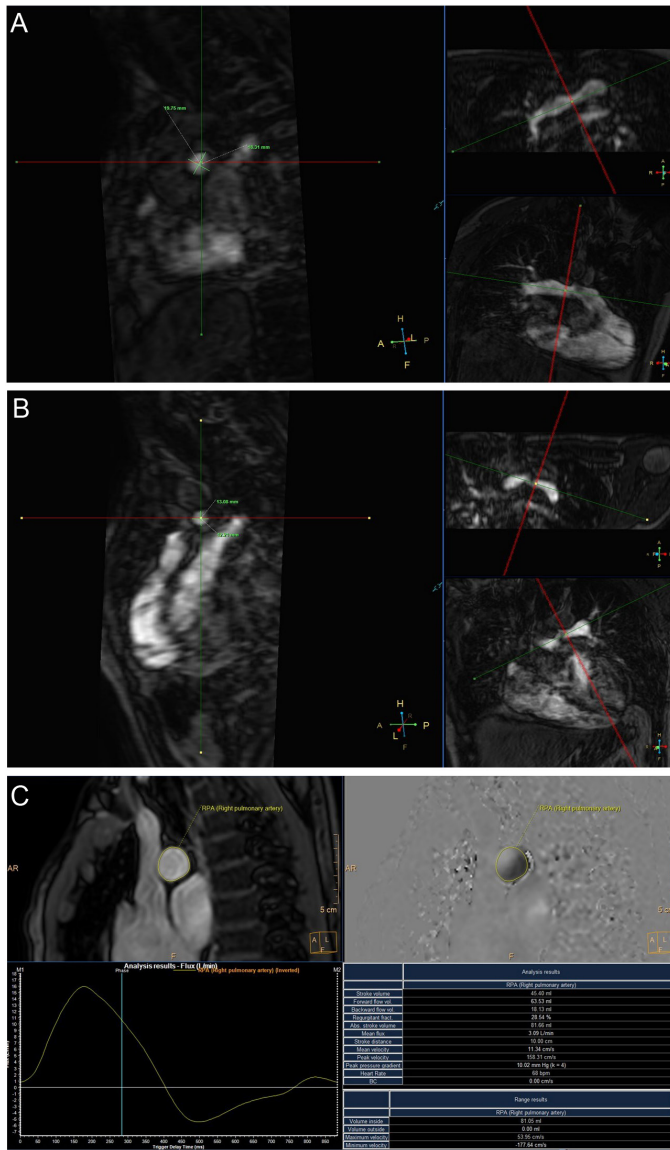
Figure 3. (A-D) A 13-year-old male patient with repaired tetralogy of Fallot. Measurement of the right pulmonary artery (A) and left pulmonary artery (B) in multiplanar reconstructed images of MRA. Phase contrast MRI measurement for the right pulmonary artery (C) and left pulmonary artery (D). The area for the right and left pulmonary arteries are calculated as 283 mm² ((3.14 × 19.7 × 18.3)/4) and 125 mm² ((3.14 × 12.2 × 13.1)/4), respectively. The narrowed-to-total pulmonary artery area ratio is calculated as 0.31 (125/407). Net right and left pulmonary artery flows are measured as 45 mL and 21 mL, respectively. The right-to-left pulmonary artery flow ratio is calculated as 68/32%, accepted as a diminished preferential pulmonary flow towards the left lung.

Fontan-like circulation. The role of phase-contrast MRI and other non-invasive imaging techniques in diagnosing branch pulmonary artery stenosis is growing in importance.[12] Studies have demonstrated the accuracy of phase-contrast MRI in correlating differential blood flow with lung scintigraphy in adults with normal branch pulmonary artery anatomy.[13] Furthermore, recent research has provided robust documentation of branch pulmonary artery blood flow in patients with pulmonary incompetence, highlighting its value in this population.[14,20,21]

Although MRA has demonstrated a strong correlation with the gold-standard invasive catheter angiography in assessing the great vascular

Table 1. Demographic Findings and the Details of the Branch Pulmonary Artery Measurements of the Study Cohort

Parameters	Control Group	BPA Stenosis Group	P
Number of Patients (n)	136	136	–
Male: Female Ratio	83:53 (1.5:1)	84:52 (1.6:1)	–
Median Age (years)	15.5 (12-22)	16 (11-20)	–
Pulmonary Artery Diameter			
RPA Diameter (mm)	17 (2-20)	15 (5-15)	.522
LPA Diameter (mm)	15(5-18)	12.5(5-16)	.006*
Pulmonary Artery Cross Sectional Area			
RPA Area (mm²)	209.5 (73-314)	164 (64-314)	.459
LPA Area (mm²)	176 (73-296)	113 (52-225)	.002*
Pulmonary Artery Diameter Z-score			
RPA Z-score	1.96 (1.08-2.23)	1.57 (0.89-2.80)	.317
LPA Z-score	1.49 (0.45-2.12)	1.96 (-0.53-1.57)	<.00001

Results are presented as median (Interquartile range, 25th–75th percentiles). *P* is the *P*-value of Mann–Whitney *U* test analysis.

BPA, branch pulmonary artery; LPA, left pulmonary artery; RPA, right pulmonary artery.

*P value is significant if <.05.

structures, offering the benefit of avoiding both radiation exposure and iodinated contrast agents.[11] Ordovás et al[9] also demonstrated that the right-to-left pulmonary artery diameter ratio fails to predict flow discrepancies. Greenberg et al[22] suggested that branch pulmonary arteries are usually oval-shaped, potentially leading to inaccuracies in single-diameter measurement methods. The non-circular shape of the branch pulmonary artery and the findings of Greenberg et al[22] provide methodological support for using cross-sectional area measurements in this study, ensuring greater accuracy in evaluating stenosis severity. The current study introduces a more robust approach: the BPA-ratio, calculated as the narrowed-to-total pulmonary artery cross-sectional area, to establish a clinically useful threshold for intervention.

This ratio serves as a reliable indicator of branch pulmonary artery stenosis, offering a clear threshold that can be used to determine the need for intervention. The results indicate that negative test outcomes demonstrate high accuracy in excluding branch pulmonary artery stenosis, which reduces the need for phase-contrast MRI and its associated technical limitations, thereby preventing unnecessary invasive

Table 2. Comparison of Narrowed-to-Total BPA Area Ratio of the Control and the BPA Stenosis Groups by Age Groups

Study Groups		N	Narrowed-to-Total BPA Area Ratio	P
Total	**Control**	136	0.46 (0.43-0.48)	<.00001
	BPA stenosis	136	0.38 (0.32-0.42)	
Group 1 (2-8 years)	**Control**	9	0.48 (0.44-0.50)	.002
	BPA stenosis	9	0.34 (0.28-0.41)	
Group 2 (9-18 years)	**Control**	81	0.45 (0.43-0.48)	<.00001
	BPA stenosis	81	0.39 (0.34-0.43)	
Group 3 (19-30 years)	**Control**	32	0.45(0.43-0.48)	<.00001
	BPA stenosis	32	0.37 (0.32-0.42)	
Group 4 (31- years)	**Control**	14	0.45 (0.43-0.47)	.00016
	BPA stenosis	14	0.34 (0.24-0. 38)	

Results are presented as median (Interquartile range, 25th–75th percentiles). *P* is the *P*-value of Mann–Whitney *U* test analysis.

BPA, branch pulmonary artery; LPA, left pulmonary artery; RPA, right pulmonary artery.

*P value is significant if <.05.
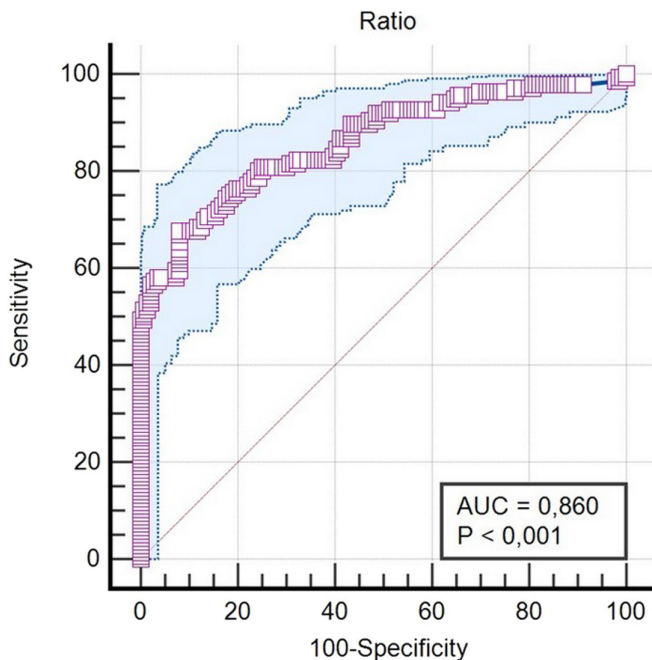
Figure 4. A discriminative narrowed-to-total pulmonary artery area ratio ≤ 0.40 demonstrates a positive predictive value of 70.5% and a negative predictive value of 80.99% for identifying branch pulmonary artery stenosis in repaired tetralogy of Fallot. This threshold's receiver operating characteristic (ROC) curve yields an area under the curve (AUC) of 0.85, indicating its strong utility in ruling out branch pulmonary artery stenosis.

procedures. Conversely, positive results are clinically significant and should be corroborated with confirmatory tests, such as phase-contrast MRI or perfusion scintigraphy. The ratio provides valuable support in classifying patients and enhancing the treatment process. By establishing a precise ratio that correlates with clinically significant stenosis, the study offers a useful tool for clinicians, enabling them to make informed decisions regarding the timing and treatment options.

Another significant contribution of this study is the introduction of the branch-to-total pulmonary artery area ratio as a practical diagnostic metric. MRA offers a non-invasive alternative to evaluate the severity of branch pulmonary artery stenosis without ionizing radiation or radionuclides, making it a practical tool in routine radiology practice.

Magnetic resonance imaging is an appropriate cross-sectional imaging modality for long-term follow-up, particularly in patients with congenital heart disease, as it enables comprehensive evaluation of simultaneous anatomical and physiological changes without radiation exposure. Additionally, it allows for monitoring disease progression and assessing intervention effectiveness over time, thereby supporting long-term patient management.

The study has several limitations, including its retrospective nature, single-center, and small sample size study population. Further research involving prospective data from multiple institutions in large patient cohorts would be valuable in various populations. Another limitation is the lack of confirmation of branch pulmonary artery stenosis through cardiac catheterization or lung scintigraphy. However, obtaining such confirmation would be particularly challenging, especially for the control group, as these procedures involve deep sedation or

anesthesia in young children and exposure to radiation and radionuclides. These ethical considerations could render such a study unfeasible. Furthermore, the study population was inherently selective, as all participants had congenital pulmonary arterial stenoses and were referred for MRI to assess hemodynamic significance. The inter- or intraobserver variability was not assessed in this study as phase-contrast MRI is a well-validated technique.[13,14] Additionally, all cardiac MRI examinations were performed using an institutionally approved clinical protocol and evaluated by experienced radiologists in cardiovascular imaging.[21,23] Another limitation of this study is that the estimated area was calculated using the ellipse area formula based on 2 diameters. However, area measurements obtained from multiplanar reconstructions would increase the software dependence. In a busy radiology practice, calculating the area using the ellipse formula may offer a more practical alternative.

In conclusion, a narrowed branch-to-total pulmonary artery area ratio of 0.40, measured using cross-sectional imaging, can assist in identifying patients who may require catheter angiography, mainly when cardiac MRI is unavailable or flow measurement is not feasible. This study refines an existing methodology by incorporating both morphological and flow-based parameters in stenosis evaluation. It can serve as a valuable reference in daily radiology practice, guiding the referral of patients for further investigations without the need for radiation exposure or advanced traditional imaging techniques.

REFERENCES
1. Villafañe J, Feinstein JA, Jenkins KJ, et al. Hot topics in tetralogy of Fallot. *J Am Coll Cardiol*. 2013;62(23):2155-2166. [CrossRef]
2. Bacha EA, Kreutzer J. Comprehensive management of branch pulmonary artery stenosis. *J Interv Cardiol*. 2001;14(3):367-375. [CrossRef]
3. Maskatia SA, Spinner JA, Morris SA, Petit CJ, Krishnamurthy R, Nutting AC. Effect of branch pulmonary artery stenosis on right ventricular volume overload in patients with tetralogy of Fallot after initial surgical repair. *Am J Cardiol*. 2013;111(9):1355-1360. [CrossRef]
4. Rhodes J, Dave A, Pulling MC, et al. Effect of pulmonary artery stenoses on the cardiopulmonary response to exercise following repair of tetralogy of Fallot. *Am J Cardiol*. 1998;81(10):1217-1219. [CrossRef]
5. Hiremath G, Qureshi AM, Meadows J, Aggarwal V. Treatment approach to unilateral branch pulmonary artery stenosis. *Trends Cardiovasc Med*. 2021;31(3):179-184. [CrossRef]

6. Fontan F, Fernandez G, Costa F, et al. The size of the pulmonary arteries and the results of the Fontan operation. *J Thorac Cardiovasc Surg*. 1989;98(5 Pt 1):711-724. **[CrossRef]**

7. Girod DA, Rice MJ, Mair DD, Julsrud PR, Puga FJ, Danielson GK. Relationship of pulmonary artery size to mortality in patients undergoing the Fontan operation. *Circulation*. 1985;72(3 Pt 2):II93-II96.

8. Senzaki H, Kato H, Akagi M, Hishi T, Yanagisawa M. Relationship between the pulmonary artery index and physiological properties of the pulmonary vascular bed. *Jpn Circ J*. 1996;60(6):334-340. **[CrossRef]**

9. Ordovás KG, Tan C, Reddy GP, Weber OM, Lu Y, Higgins CB. Disparity between ratios of diameters and blood flows in central pulmonary arteries in postoperative congenital heart disease using MRI. *J Magn Reson Imaging*. 2007;25(4):721-726. **[CrossRef]**

10. Sridharan S, Derrick G, Deanfield J, Taylor AM. Assessment of differential branch pulmonary blood flow: a comparative study of phase contrast magnetic resonance imaging and radionuclide lung perfusion imaging. *Heart*. 2006;92(7):963-968. **[CrossRef]**

11. Valsangiacomo Büchel ER, DiBernardo S, Bauersfeld U, Berger F. Contrast-enhanced magnetic resonance angiography of the great arteries in patients with congenital heart disease: an accurate tool for planning catheter-guided interventions. *Int J Cardiovasc Imaging*. 2005;21(2-3):313-322. **[CrossRef]**

12. Fratz S, Chung T, Greil GF, et al. Guidelines and protocols for cardiovascular magnetic resonance in children and adults with congenital heart disease: SCMR expert consensus group on congenital heart disease. *J Cardiovasc Magn Reson*. 2013;15(1):51. **[CrossRef]**

13. Silverman JM, Julien PJ, Herfkens RJ, Pelc NJ. Quantitative differential pulmonary perfusion: MR imaging versus radionuclide lung scanning. *Radiology*. 1993;189(3):699-701. **[CrossRef]**

14. Kang IS, Redington AN, Benson LN, et al. Differential regurgitation in branch pulmonary arteries after repair of tetralogy of Fallot: a phase-contrast cine magnetic resonance study. *Circulation*. 2003;107(23):2938-2943. **[CrossRef]**

15. Feltes TF, Bacha E, Beekman RH 3rd, et al. American Heart Association Congenital Cardiac Defects Committee of the Council on Cardiovascular Disease in the Young, Council on Clinical Cardiology, Council on Cardiovascular Radiology and Intervention, American Heart Association. Indications for cardiac catheterization and intervention in pediatric cardiac disease: a scientific statement from the American Heart Association. *Circulation*. 2011;123(22):2607-2652. **[CrossRef]**

16. Pruckmayer M, Zacherl S, Salzer-Muhar U, Schlemmer M, Leitha T. Scintigraphic assessment of pulmonary and whole-body blood flow patterns after surgical intervention in congenital heart disease. *J Nucl Med*. 1999;40(9):1477-1483.

17. Dowdle SC, Human DG, Mann MD. Pulmonary ventilation and perfusion abnormalities and ventilation perfusion imbalance in children with pulmonary atresia or extreme tetralogy of Fallot. *J Nucl Med*. 1990;31(8):1276-1279.

18. Alderson PO, Boonvisut S, McKnight RC, Hartman AF Jr. Pulmonary perfusion abnormalities and ventilation-perfusion imbalance in children after total repair of tetralogy of Fallot. *Circulation*. 1976;53(2):332-337. **[CrossRef]**

19. Fratz S, Hess J, Schwaiger M, Martinoff S, Stern HC. More accurate quantification of pulmonary blood flow by magnetic resonance imaging than by lung perfusion scintigraphy in patients with Fontan circulation. *Circulation*. 2002;106(12):1510-1513. **[CrossRef]**

20. Wu M-T, Huang Y-L, Hsieh K-S, et al. Influence of pulmonary regurgitation inequality on differential perfusion of the lungs in tetralogy of Fallot after repair: a phase-contrast magnetic resonance imaging and perfusion scintigraphy study. *J Am Coll Cardiol*. 2007;49(18):1880-1886. **[CrossRef]**

21. Ozkok S, Tosun O, Yucel IK, Celebi A. Cardiac MRI in surgically repaired tetralogy of Fallot: our initial experience. *North Clin Istanb*. 2022;9(6):622-631. **[CrossRef]**

22. Greenberg SB, Lang SM, Gauss CH, Lensing SY, Ali S, Lyons KA. Normal pulmonary artery and branch pulmonary artery sizes in children. *Int J Cardiovasc Imaging*. 2018;34(6):967-974. **[CrossRef]**

23. Ozkok S, Erdemli S, Aslan A, Kabaalioglu A. Measurement of heart chambers and mediastinal vascular structures on raw axial chest MDCT in the pediatric age group. *Eur J Anat*. 2021;25(6):633-644.

Assessment of Meniscal Pathologies and Meniscal Volume Quantification in Individuals with and without Radiographic Osteoarthritis

Özge Tanişman[1] , Eren Tobcu[2] , Bilgin Topcu[2] , Erdal Karavaş[2]

[1]Department of Radiology, Bandırma Training and Research Hospital Balıkesir, Türkiye
[2]Department of Radiology, Bandırma Onyedi Eylül University School of Medicine, Bandırma Research and Training Hospital, Balıkesir, Türkiye

Abstract

Objective: The purpose of this study is to determine whether osteoarthritis (OA) is associated with meniscus volume and pathologies in young and middle-aged individuals.

Methods: This study assessed 155 knee magnetic resonance images (MRIs) and X-rays from 138 participants aged 18-65. The knee X-ray examination was employed to identify OA, whereas the knee MRI was utilized to evaluate meniscal diseases. The volume of the meniscus was measured using ITK-SNAP software.

Results: There was a strong correlation between age and OA ($P < .001$). A link was identified between medial and lateral meniscus disease and age ($P < .001$, $P = .002$, respectively). Osteoarthritis was identified as being linked to both medial and lateral meniscus diseases ($P < .001$, $P = .007$ respectively). Medial meniscus extrusion was identified as being correlated with OA ($P < .001$). Neither medial nor lateral meniscus volumes showed significant correlations with OA ($P = .236$, $P = .501$ respectively). The inter-reader agreement for meniscal volume measurements was assessed using intraclass correlation coefficients (ICCs). ICCs for inter-reader agreement was 0.84.

Conclusion: In cases of meniscal disorders, including meniscal extrusion, even in the absence of OA symptoms, the patient should be considered at risk for OA and monitored accordingly. Given the aging population that is predicted to rise over the next several years, this strategy will also help to manage the condition more affordably.

Keywords: ITK-SNAP, meniscus volume, osteoarthritis

INTRODUCTION

Knee osteoarthritis (OA) is a complex, multifactorial condition that impacts the entire joint and is a leading cause of disability globally.[1] Osteoarthritis, a prevalent degenerative musculoskeletal disorder, is associated with numerous risk factors including advanced age, female sex, malalignment, obesity, genetic predispositions, and trauma.[2,3] Osteoarthritis is a prevalent source of pain and impairment in the aged population.[4] Given the rising older population due to increased life expectancy, the significance of this disease will escalate in the coming decades. An essential first step in preventing this disease, which impacts both individuals and society, is to comprehend it and identify its risk factors and causes.

The growing acknowledgment of the relationships among the structural tissues of the knee joint has led researchers to classify several OA phenotypes based on biochemical and imaging results.[5] Articular cartilage degeneration and changes in subchondral bone are the leading biomarkers of OA.[6] The meniscus is a fibrocartilaginous structure that is crucial for absorbing, transferring, and dispersing mechanical stress within the knee joint. It has been demonstrated that the lack of a functional meniscus exposes the knee's articular cartilage to pathologic stresses, leading to degeneration.[7,8] A robust causal link between meniscus injury and the structural development of OA is well acknowledged.[9] Therefore, especially when investigating knee OA, it is important to evaluate the joint space, subchondral sclerosis, and osteophytes, as well as assess meniscus pathologies, particularly in early-stage cases.

Research has been attempted to elucidate the influence of meniscal modifications on the start of OA, emphasizing factors such as volume, extrusion, thickness (height), and tibial coverage that describe meniscal architecture.[10-12] In the magnetic resonance imaging (MRI) Osteoarthritis Knee Score, extrusion and meniscal morphology were rated as semi-quantitative parameters.[13] However, meniscus volume is not yet included in this scoring system.

Liu et al[14] and Atik et al[15] have conducted studies revealing the relationship between meniscus structure, pathologies, and OA in elderly patients. Given that advanced age is a risk factor for OA, the study was designed to focus on young and middle-aged adults. Thus, the aim was to examine the correlation between meniscus pathology and OA while controlling for the positive impact of age on the progression of OA. The purpose of this study is to determine whether OA is associated with meniscus volume and pathologies in young and middle-aged individuals.

METHODS
Study Population
This is a single-center, retrospective, and cross-sectional study. This research has been approved by the ethical committee of Bandırma Onyedi Eylül University School of Medicine(Decision: January 2, 2025, no: 2024-12-05). The study was conducted in acordance with the Declaration of Helsinki. Written informed consent was obtained from patients who participated in this study.

Patients who underwent knee MRI at the hospital from December 2023 to June 2024 were retrospectively examined using Picture Archiving and Communication Systems. Patients aged 18-65 who had both knee MRI and knee radiography (RG) were identified. The study excluded trauma patients, individuals who had knee surgery for any reason, those with metabolic disorders, osteoporotic patients, oncology patients, and patients with suboptimal imaging quality. The screening resulted in the inclusion of 155 knee MRIs and knee X-rays from 138 participants aged 18-65 in the research.

Radiological Evaluation
This study analyzed Anteroposterior (AP) knee RG in the extended position. The RGs were evaluated using the Kellgren Lawrence (KL) classification system for OA. Accordingly, grade 0 is normal; grade 1 is suspicious osteophyte formation; grade 2 is significant osteophyte formation with normal joint space; grade 3 is osteophytes, narrowing of the joint space, and subchondral sclerosis; grade 4 is a reduction in joint space or ankylosis with multiple osteophytes, significant sclerosis, and erosion.[16] Patients were classified as having knee OA if their KL score was greater than or equal to 2. Patients were categorized into 2 groups according to the presence or absence of OA (Figure 1). The assessment was performed by 2 experienced radiologists. In instances of interpretative inconsistency or ambiguous cases, the images were re-assessed, and a consensus final decision was reached. The knee RG was used to measure the joint space.

Magnetic resonance imaging (MRI) was used to assess meniscus diseases. All MR images were acquired using a 1.5 Tesla MRI device (GE 1.5T, 60 cm, SIGNA™ Creator/Explorer, China, 2017). The MRI

evaluation was conducted with the knee in an extended posture. The assessment was performed utilizing a knee MRI protocol including coronal T1, sagittal fat-suppressed proton-weighted, coronal fat-suppressed proton-weighted, and axial fat-suppressed proton-weighted sequences. The anterior and posterior horns of the lateral and medial menisci were assessed individually for each knee. Patients were categorized into 3 groups according to the condition of their meniscus: normal, degenerated, or torn. In addition, the presence of extrusion in the meniscus was evaluated with the coronal plane of MRI. Unaware of the patients' clinical and X-ray scans, 2 experienced radiologists prospectively reinterpreted each MRI. When there were uncertain or inconsistent interpretations, the images were reexamined, and a final conclusion was made by consensus.

The ITK-SNAP software was employed to evaluate the volume of the meniscus.[17] Magnetic resonance scans were uploaded to the software, and measurements were obtained using a three-dimensional (3D) region of interest. Measurements were obtained in the sagittal plane and subsequently validated with additional sequences. Segmentation was conducted from lateral to medial on all sections where the meniscus was visible (Figure 2). The volume measures were conducted independently by 2 radiologists who were oblivious to the patient's radiological results.

Statistical Analysis
Descriptive statistics were applied to analyze the baseline characteristics. The Chi-square (χ^2) test and Fisher's exact χ^2 test were applied in the evaluation of qualitative data. After testing for normality, statistical significance was calculated using an independent sample t-test for comparisons between 2 groups or one-way ANOVA for comparisons among 3 or more groups when the data were normally distributed. For non-normally distributed data, the Mann–Whitney U test was used for 2-group comparisons, and the Kruskal–Wallis test was applied for 3 or more groups. The Pearson correlation test was used to assess the linear relationship between normally distributed continuous variables, while the Spearman correlation test was used for those without a normal distribution. Interobserver agreement was assessed using the intraclass correlation coefficient (ICC). The significance of the ICC values was interpreted as follows: <0.50 poor, 0.50-0.75 moderate, 0.75-0.90 good, and >0.90 excellent reliability. All statistical analyses were performed using IBM SPSS software (IBM SPSS Corp.; Armonk, NY, USA, version 23), and a significance level of $P < .05$ was considered.
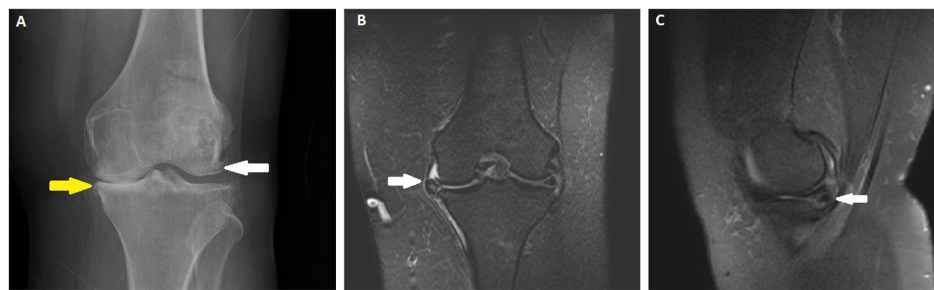
RESULTS
There were 57 (36.7%) male patients and 98 (63.2%) female patients. In this investigation, radiographic evidence of knee OA was identified in 84 (54.1%) of the 155 cases evaluated (KL grade $\geq$ 2). The characteristics of the study group are presented in Table 1.

There was a strong correlation between age and OA ($P < .001$). It was found that as people age, OA becomes more common. There was a correlation found between gender and OA ($P = .004$). Osteoarthritis is more frequently detected in females. A link was identified between medial and lateral meniscus disease (degeneration and tear) and age ($P < .001$, $P = .002$, respectively). The prevalence of medial meniscus disease was higher. Osteoarthritis was identified as being linked to both medial and lateral meniscus diseases ($P < .001$, $P = .007$ respectively). Medial meniscus extrusion was identified as being correlated with OA ($P < .001$). Lateral meniscus extrusion was not significantly associated with OA ($P = .5$). Medial meniscus diseases and medial joint space

Figure 1. A 56-year-old female patient. The RG of the knee showed OA (A). Subchondral sclerosis (yellow arrow), joint space narrowing (yellow arrow), and osteophyte formation (white arrow) are noted. The fat-suppressed proton density-weighted MR sequence indicates medial meniscus extrusion in the coronal plane (B) and a horizontal tear of the posterior horn of the medial meniscus in the sagittal plane (C), as shown by arrows.
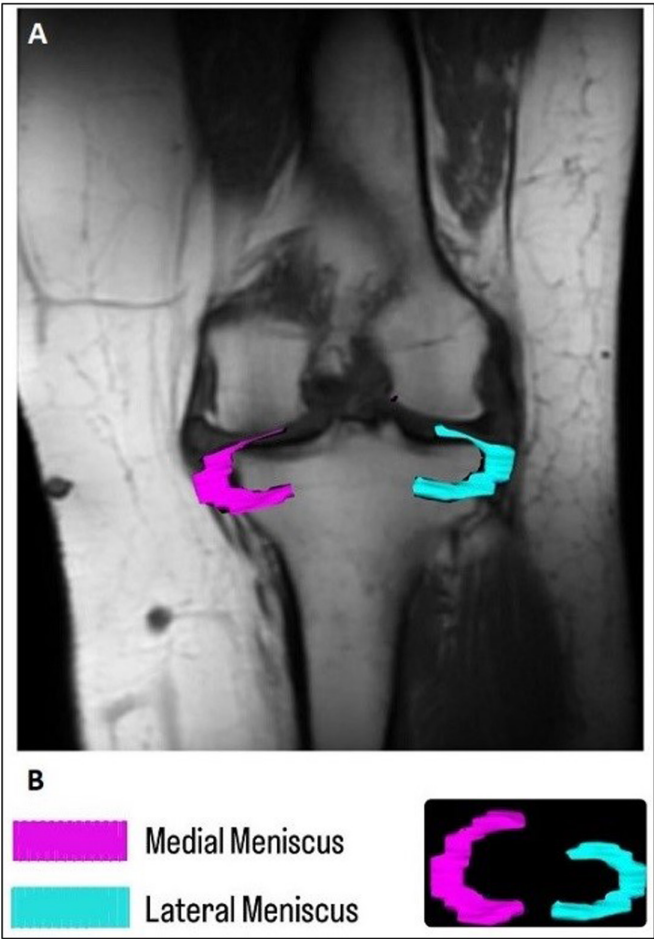
were found to be significantly correlated ($P < .015$). A correlation was demonstrated between gender and the volume of the medial and lateral meniscus ($P < .001$). The volume of the meniscus was determined to be larger in males. Neither medial nor lateral meniscus volumes showed significant correlations with OA ($P = .236$, $P = .501$ respectively) (Table 2). The inter-reader agreement was assessed for meniscal volume measurements using ICCs. Intraclass correlation coefficient for interreader agreement was 0.84.

Figure 2. Example of meniscus segmentation. (A) Three-dimensional representation of the left knee and coronal perspective of meniscus segmentation. (B) Meniscus in 3D from segmentation (lateral meniscus is blue; medial meniscus is purple).

DISCUSSION

Knee OA is a degenerative musculoskeletal disease that can be caused by a variety of reasons. Radiography is used to make the diagnosis of OA. Osteoarthritis results can also be assessed using MRI. Meniscus diseases present a substantial risk for the onset and advancement of OA and are relatively common in knee MRI studies.[18]

Radiography was used to evaluate knee OA in this study. Knee OA was diagnosed in 54.1% of patients, with a notable increase in frequency associated with advancing age. This study revealed that women exhibited OA outcomes more frequently than males. It was discovered that these findings aligned with previous research.[2,3,15]

In this study, it was discovered that meniscus diseases are more common in people with OA than in those without OA, and they also increase with age. It was found that 54.9% of individuals without OA had meniscus pathology, whereas 82.1% of patients with OA had meniscus pathology. In studies that include elderly patients in the study group, these rates are elevated.[15,19] In contrast to these studies, the

Table 1. Patient Characteristics and Features of the Knee Joint

Characteristics	n=155
Age, mean (range) years	45.6 (19-64)
Gender female/male (%)	98 (63.2%)/57 (36.7%)
OA (%)	
Yes	84 (54.1%)
No	71 (45.8%)
Medial joint space, mean (range) mm	5.2 (1.53-12.8)
Lateral joint space, mean (range) mm	6.1 (2.28-11.3)
Medial meniscus (%)	
Normal	47 (30.2%)
Degeneration	71 (45.8%)
Tear	37 (23.8%)
Lateral meniscus (%)	
Normal	126 (81.2%)
Degeneration	20 (12.9%)
Tear	9 (5.8%)
Medial meniscus extrusion	
Yes	34 (21.9%)
No	121 (78%)
Lateral meniscus extrusion	
Yes	2 (1.2%)
No	153 (98.7%)
Medial meniscus volume, mean (range) mm^3	1745 (964-3822)
Lateral meniscus volume, mean (range) mm^3	1317 (552-2905)

OA, osteoarthritis.

Table 2. The Relationship Between Osteoarthritis and the Other Parameters

	Patient with OA N[a], Mean[b]	Patient without OA N[a], Mean[b]	P
Age[b]	52	37	<.001*
Gender[a]			
Female	62	36	.004*
Male	22	35	
Medial meniscus disease[a]	69	39	.007*
Lateral meniscus disease[a]	23	6	<.001*
Medial meniscus volüme (mm³)[b]	1793	1689	.236
Lateral meniscus volume (mm³)[b]	1298	1341	.501
Medial meniscus extrusion[a]	31	3	<.001*
Lateral meniscus extrusion[a]	2	0	.5

OA, osteoarthritis.

*$P < .05$.

There are numbers and average values in this data. For example, among those marked with a, there are 62 women with oa, while the average age ofpatients with oa (marked with b) is 52.

I noticed a mistake in the numbers in the age line. I corrected that too.

reduced prevalence of meniscus pathology in patients without OA in this research can be attributed to the fact that the patients were under 65 years of age.

The prevalence of medial meniscus pathology was higher than that of lateral meniscus diseases. Compared to the lateral meniscus, the medial meniscus is more vulnerable to injury and extrusion because of its anatomical characteristics and relative lack of mobility.[20] The increased prevalence of medial meniscus diseases relative to the lateral meniscus in the current study has been linked to this condition.

A strong correlation between OA and medial meniscus extrusion was discovered. Medial meniscus extrusion was seen more often in patients with OA than in those without the condition. In a review made by Ghouri et al[21], it was identified that meniscal extrusion is a risk factor for knee OA cartilage structural progression independently of age, gender, and BMI.

Osteoarthritis and both medial and lateral meniscus volume did not significantly correlate in the current research. Previous studies indicate that a greater initial meniscal volume and alterations in volume over time are associated with OA.[22,23] Individual anatomical variations in the meniscus have been documented in healthy knees.[24] To the authors' knowledge, there is no established normal range for meniscus volume for this reason. Given the absence of a standard range for meniscus volume, it was determined that a solitary measurement in a cross-sectional study would be inadequate and that temporal changes would provide more significant knowledge. This has been assumed to be the cause of the lack of any correlation between OA and meniscus volume.

A theory states that the extruded meniscus outside the joint edge has the chance to expand since the bones that comprise the joint do not compress it.[25] Okazaki et al[26] and Nebelung et al[27] established that alterations in meniscus volume, both in vitro and in vivo, could be triggered by variations in load on the meniscus. Baseline meniscus extrusion was positively correlated with changes in meniscus volume, according to Xu et al[23], but they found no correlation between changes in meniscus volume and radiographic knee OA. It can be concluded from this data that changes in meniscus volume are not the mechanism by which meniscus extrusion affects OA. Therefore, it is possible to think that

an extrusion of the meniscus first leads to a larger meniscus, which then causes radiographic knee OA. According to Xu et al[23], this theory requires testing in cohorts with younger participants.

The findings of this investigation, which excluded those aged 65 and older, confirm that meniscal extrusion influences OA before alterations in meniscus volume occur. Nevertheless, due to the retrospective nature of this investigation, the impact of extrusion on meniscus volume could not be assessed. This hypothesis requires validation through extensive randomized controlled studies, including young patients.

There were several limitations to this study. The main limitation of this study is its retrospective design. The impact of temporal variations in meniscus volume on OA was not detected. The second limitation is that clinical findings and concerns from patients were not included in the study. Thirdly, the actual incidence of meniscal extrusion may be understated because all MRI studies evaluated extrusion while the subject was supine and not bearing any weight.

Osteoarthritis impacts the entire joint and is a leading cause of disability globally. Thus, it is critical to identify it early and restrict its progression. In cases of meniscal disorders, including meniscal extrusion, even in the absence of OA symptoms, the patient should be considered at risk for OA and monitored accordingly. Given the aging population that is predicted to rise over the next several years, this strategy will also help to manage the condition more affordably.

REFERENCES
1. Gao KT, Xie E, Chen V, et al. Large-scale analysis of meniscus morphology as risk factor for knee osteoarthritis. *Arthritis Rheumatol*. 2023;75(11):1958-1968. [CrossRef]
2. Jang S, Lee K, Ju JH. Recent updates of diagnosis, pathophysiology, and treatment on osteoarthritis of the knee. *Int J Mol Sci*. 2021;22(5):2619. [CrossRef]
3. Magnusson K, Turkiewicz A, Snoeker B, Hughes V, Englund M. The heritability of doctor-diagnosed traumatic and degenerative meniscus tears. *Osteoarthr Cartil*. 2021;29(7):979-985. [CrossRef]
4. Anderson AS, Loeser RF. Why is OA an age-related disease? *Best Pract Res Clin Rheumatol*. 2010;24(1):15-26. [CrossRef]
5. Roemer FW, Collins J, Kwoh CK, et al. MRI-based screening for structural definition of eligibility in clinical DMOAD trials: Rapid Osteoarthritis MRI Eligibility Score (ROAMES). *Osteoarthr Cartil*. 2020;28(1):71-81. [CrossRef]
6. Shrive NG, O'Connor JJ, Goodfellow JW. Load-bearing in the knee joint. *Clin Orthop Relat Res*. 1978 Mar-Apr;(131):279-287. [CrossRef]

7.   Hede A, Larsen E, Sandberg H. The long term outcome of open total and partial meniscectomy related to the quantity and site of the meniscus removed. *Int Orthop*. 1992;16(2):122-125. **[CrossRef]**

8.   Jaureguito JW, Elliot JS, Lietner T, Dixon LB, Reider B. The effects of arthroscopic partial lateral meniscectomy in an otherwise normal knee: a retrospective review of functional, clinical, and radiographic results. *Arthroscopy*. 1995;11(1):29-36. **[CrossRef]**

9.   Sharma L, Eckstein F, Song J, et al. Relationship of meniscal damage, meniscal extrusion, malalignment, and joint laxity to subsequent cartilage loss in osteoarthritic knees. *Arthritis Rheum*. 2008;58(6):1716-1726. **[CrossRef]**

10.   Siorpaes K, Wenger A, Bloecker K, Wirth W, Hudelmaier M, Eckstein F. Interobserver reproducibility of quantitative meniscus analysis using coronal multiplanar DESS and IWTSE MR imaging. *Magn Reson Med*. 2012;67(5):1419-1426. **[CrossRef]**

11.   Wirth W, Frobell RB, Souza RB, et al. A three-dimensional quantitative method to measure meniscus shape, position, and signal intensity using MR images: a pilot study and preliminary results in knee osteoarthritis. *Magn Reson Med*. 2010;63(5):1162-1171. **[CrossRef]**

12.   Bowers ME, Tung GA, Fleming BC, Crisco JJ, Rey J. Quantification of meniscal volume by segmentation of 3T magnetic resonance images. *J Biomech*. 2007;40(12):2811-2815. **[CrossRef]**

13.   Hunter DJ, Guermazi A, Lo GH, et al. Evolution of semi-quantitative whole joint assessment of knee OA: MOAKS (MRI Osteoarthritis Knee Score). *Osteoarthr Cartil*. 2011;19(8):990-1002. **[CrossRef]**

14.   Liu Y, Du G, Liu J. Meniscal anterior and posterior horn heights are associated with MRI-defined knee structural abnormalities in middle-aged and elderly patients with symptomatic knee osteoarthritis. *BMC Musculoskelet Disord*. 2022;23(1):1-10. **[CrossRef]**

15.   Atik I, Gul E, Atik S. Evaluation of the relationship between Knee osteoarthritis and meniscus Pathologies. *Malawi Med J*. 2024;36(1):48-52. **[CrossRef]**

16.   Kellgren JH, Lawrence JS. Radiological assessment of osteo-arthrosis. *Ann Rheum Dis*. 1957;16(4):494-502. **[CrossRef]**

17.   Yushkevich PA, Piven J, Hazlett HC, et al. User-guided 3D active contour segmentation of anatomical structures: significantly improved efficiency and reliability. *Neuroimage*. 2006;31(3):1116-1128. **[CrossRef]**

18.   Aylanç N, Ertem ŞB. Medial meniskal ekstrüzyon İLE dejeneratİf artrİtİn NEDEN SONUÇ İLİŞKİSİ bakimindan İncelenmesİ investigation of the cause-effect relationship between degenerative arthritis and medial meniscal extrusion. *Bozok Tıp Derg*. 2020;10(2):16-22. **[CrossRef]**

19.   Özdemir M, Kavak R. Meniscal lesions in geriatric population: prevalence and association with knee osteoarthritis. *Curr Aging Sci*. 2019;12(1):67-73. **[CrossRef]**

20.   Papalia GF, Za P, Saccone L, et al. Meniscal extrusion: risk factors and diagnostic tools to predict early osteoarthritis. *Orthop Rev (Pavia)*. 2023;15:74881. **[CrossRef]**

21.   Ghouri A, Muzumdar S, Barr AJ, et al. The relationship between meniscal pathologies, cartilage loss, joint replacement and pain in knee osteoarthritis: a systematic review. *Osteoarthr Cartil*. 2022;30(10):1287-1327. **[CrossRef]**

22.   Xu D, Van Der Voet J, Hansson NM, et al. Association between meniscal volume and development of knee osteoarthritis. *Rheumatology (Oxford)*. 2021;60(3):1392-1399. **[CrossRef]**

23.   Xu D, van der Voet J, Waarsing JH, et al. Are changes in meniscus volume and extrusion associated to knee osteoarthritis development? A structural equation model. *Osteoarthr Cartil*. 2021;29(10):1426-1431. **[CrossRef]**

24.   Fox AJS, Wanivenhaus F, Burge AJ, Warren RF, Rodeo SA. The human meniscus: a review of anatomy, function, injury, and advances in treatment. *Clin Anat*. 2015;28(2):269-287. **[CrossRef]**

25.   Wenger A, Wirth W, Hudelmaier M, et al. Meniscus body position, size, and shape in persons with and persons without radiographic knee osteoarthritis: quantitative analyses of knee magnetic resonance images from the osteoarthritis initiative. *Arthritis Rheum*. 2013;65(7):1804-1811. **[CrossRef]**

26.   Okazaki Y, Furumatsu T, Yamauchi T, et al. Medial meniscus posterior root repair restores the intra-articular volume of the medial meniscus by decreasing posteromedial extrusion at knee flexion. *Knee Surg Sports Traumatol Arthrosc*. 2020;28(11):3435-3442. **[CrossRef]**

27.   Nebelung S, Dötsch L, Shah D, et al. functional MRi Mapping of Human meniscus functionality and its Relation to Degeneration. *Sci Rep*. 2020;10(1):2499. **[CrossRef]**

Diagnostic Importance of Computed Tomography and Magnetic Resonance Imaging in Coalescent Mastoiditis, a Severe Complication of Acute Otitis Media

Muhammet Fırat Öztepe[1] , Fatma Dilek Gökharman[2]

[1]Department of Radiology, Batman Training and Research Hospital, Batman, Türkiye
[2]Department of Radiology, Ankara Training and Research Hospital, Ankara, Türkiye

Abstract

Coalescent mastoiditis, a severe form of acute mastoiditis, involves the breakdown of bony septae in the mastoid air cells, leading to abscess formation and potential intracranial complications. Despite its rarity due to antibiotic use, timely diagnosis is critical. Computed tomography (CT) is essential for detecting bone erosion, while magnetic resonance imaging (MRI) is superior for evaluating soft tissue involvement and intracranial extensions. This case report describes a 32-year-old male with coalescent mastoiditis successfully managed with intravenous antibiotics and abscess drainage, highlighting the crucial role of imaging in guiding treatment and preventing severe complications.

**Keywords:** Coalescent mastoiditis, high-resolution CT, MRI

INTRODUCTION

Coalescent mastoiditis is a severe form of acute mastoiditis characterized by the breakdown of bony septae within the mastoid air cells, leading to the formation of abscesses and potential intracranial complications.[1] It is more common mainly in early childhood[2] This condition is often a progression from acute otitis media (AOM), particularly when initial treatment is inadequate or delayed. The frequency of coalescent mastoiditis has decreased significantly with the use of antibiotics for treating ear infections. It is now relatively rare, occurring in less than 1% of cases of AOM that progress to mastoiditis.[3] Imaging plays a crucial role in diagnosing and assessing the extent of coalescent mastoiditis. Direct radiography is insufficient to show changes in bone structure; therefore, it has a limited place in the diagnosis of coalescent mastoiditis. Instead, more advanced imaging methods, such as CT and MRI, are preferred. Computed tomography (CT) provides detailed images of bony structures, making it essential for diagnosing the erosion of mastoid air cells. Magnetic resonance imaging (MRI) is superior for evaluating soft tissue involvement and intracranial complications, such as abscesses or thrombosis.[4] Early recognition and prompt intervention are essential to prevent serious complications and improve patient outcomes. This case report highlights the imaging findings of a patient with coalescent mastoiditis and its complications.

CASE PRESENTATION

The patient provided written informed consent for their anonymized information to be included in this case report. A 32-year-old male presented to the emergency department with a 5-day history of worsening ear pain, fever, and progressive hearing loss in the left ear. Physical examination revealed a temperature of 38.5°C and tenderness and swelling over the left mastoid process.

Initial laboratory workup showed elevated white blood cell count (12 000 µL) and C-reactive protein levels (20 mg/dL), indicating an acute inflammatory response. Given the clinical suspicion of mastoiditis, a high-resolution CT scan of the temporal bones was performed. Imaging revealed destruction of the bony septae in the left mastoid air cells, opacification of the mastoid antrum, middle ear cavity, and erosion of the medial and lateral mastoid cortex. MRI with contrast was subsequently obtained to further assess the extent of the infection and its complications. The MRI demonstrated peripheral enhancing collections in the mastoid antrum. These collections showed diffusion restriction consistent with abscess. There was soft tissue inflammation inferior to the mastoid bone. There were peripheral enhanced and diffusion-restricted collections adjacent to the mastoid outer cortex, consistent with subperiosteal abscess. There was erosion of the sigmoid plate. Therefore, we suspected sigmoid sinus thrombosis; however, contrast filling in the sigmoid sinus was observed, indicating that there was no thrombosis (Figures 1 and 2).
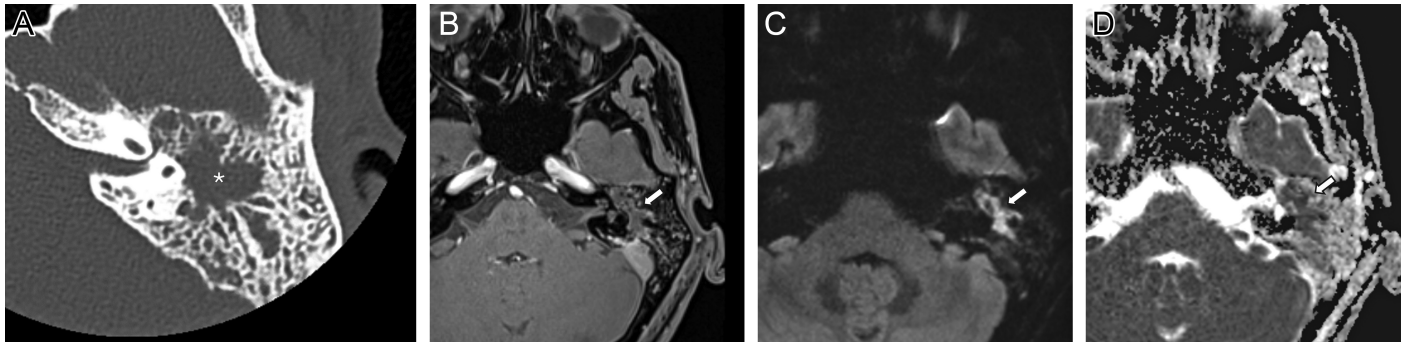
Figure 1. Axial high resolution temporal bone CT scan shows opacification and destruction of mastoid air cells. (A) Axial T1W contrast-enhanced images show peripheral contrast enhancement in the same area, (B) DWI (C) and ADC map images (D) shows diffusion restriction in this peripheral enhancing collection in mastoid air cells consistent with abscess.

The patient was admitted to the hospital and started on intravenous antibiotics, and mastoidectomy performed successfully. Postoperatively, the patient showed significant clinical improvement, with resolution of fever and reduction in ear pain and swelling. At the one-month follow-up, the patient had no residual symptoms, and repeat imaging showed complete resolution of the infection.
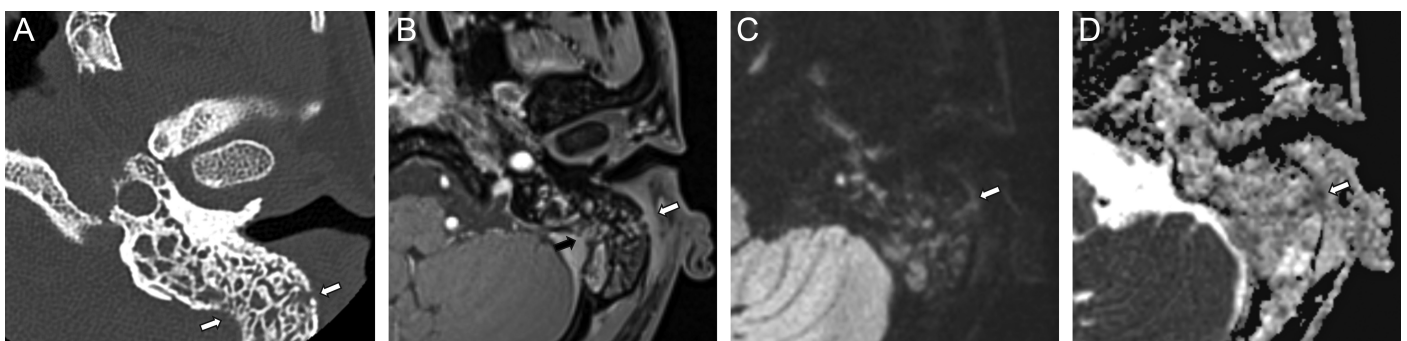
DISCUSSION

The diagnosis of coalescent mastoiditis is challenging due to its non-specific early symptoms that can be confused with less severe infections. For example, it may be confused with AOM or cellulitis, which presents with localized ear pain and tenderness. Additionally, the disease is often not recognized until severe complications arise. When imaging patients with coalescent mastoiditis, it is crucial to be vigilant

---

MAIN POINTS

- Coalescent mastoiditis is an advanced form of acute mastoiditis resulting from inadequate treatment of acute otitis media, characterized by the erosion of mastoid air cell septa and the potential for serious intracranial complications.
- Computed tomography is crucial for identifying bony destruction in the mastoid air cells, while magnetic resonance imaging is essential for assessing soft tissue involvement and ruling out intracranial complications.
- Early diagnosis and prompt treatment are vital to prevent severe outcomes and ensure patient recovery.

---

for potential complications. Thin-section CT scans are essential for detecting bone destruction and resorption of mastoid air cell septa, which indicate the severity of the infection. In our patient, extensive opacification of the mastoid air cells and widespread bone erosion were noted, extending to both the inner and outer cortex of the mastoid bone. MRI can be complementary for assessing soft tissue involvement, although it is less accurate for bone changes.[5,6] Recognizing complications such as subperiosteal abscess, facial nerve palsy, and intracranial extensions like meningitis or brain abscesses is vital for appropriate management and prognosis.[7,8] The incidence of subperiosteal abscess in coalescent mastoiditis is approximately % 50.[9-11] In contrast-enhanced sections, it is seen as a peripheral enhancing collection adjacent to the bone and restricts diffusion. If not treated, it may lead to intracranial complications. Intracranial complications have been reported between 6.8% and 23%. Facial nerve paralysis occurs due to direct inflammation of the nerve or through external pressure caused by inflammation. Labyrinthitis occurs when bacteria advance from the middle ear cavity into the labyrinth cavity through the round window. It may present as nausea, vomiting, hearing loss, dizziness, vertigo, and nystagmus.[2] In our patient, there was erosion of the outer cortex of the mastoid bone and the formation of subperiosteal abscesses in the adjacent area. Despite the erosion of the inner cortex of the mastoid bone, there was no evidence of intracranial extension of the disease.

In addition to the challenges of early diagnosis, the management of coalescent mastoiditis requires a multidisciplinary approach to address potential complications effectively. Imaging plays a pivotal role, with

Figure 2. Axial high resolution temporal bone CT scan shows destruction of the mastoid inner and outer cortex. (A) Axial T1W contrast-enhanced images show bony cortical defect and enhancement adjacent to the mastoid cortex, (B) DWI images (C) and ADC map images (D) shows diffusion restriction consistent with subperiosteal abscess. In addition, inner cortex erosion was seen (black arrow).

CT scans being crucial for assessing the extent of bone involvement and MRI providing valuable information on soft tissue structures. This comprehensive imaging approach is essential for planning appropriate surgical interventions and medical treatments. Our case highlights the importance of early and accurate imaging to detect both common and severe complications, ensuring timely and targeted management strategies.

In conclusion, coalescent mastoiditis, though rare, remains a significant clinical entity that necessitates high vigilance and expertise in diagnosis and management. The combination of imaging techniques, careful clinical monitoring, and prompt intervention can significantly improve patient outcomes. This case underscores the critical role of multidisciplinary care and the need for continuous vigilance in patients presenting with symptoms suggestive of severe ear infections. Early recognition and treatment are paramount to preventing the potentially devastating complications associated with coalescent mastoiditis.

Data Availability Statement: The data that support the findings of this study are available on request from the corresponding author.

Informed Consent: Written informed consent was obtained from the patient who agreed to take part in the study.

Peer-review: Externally peer-reviewed.

Author Contributions: Concept – M.F.Ö.; Design – M.F.Ö.; Supervision – M.F.Ö., F.D.G.; Resources – F.D.G.; Materials – F.D.G.; Data Collection and/or Processing – F.D.G.; Analysis and/or Interpretation – F.D.G.; Literature Search – M.F.Ö.; Writing Manuscript – M.F.Ö.; Critical Review – M.F.Ö.

Declaration of Interests: The authors have no conflict of interest to declare.

REFERENCES
1. Sahi D, Nguyen H, Callender KD. *Mastoiditis*; 2024.
2. Mansour S, Magnan J, Nicolas K, Haidar H. Acute otitis media and acute coalescent mastoiditis. In: *Middle Ear Diseases*. Springer International Publishing; 2018:85-113. [CrossRef]
3. Spiegel JH, Lustig LR, Lee KC, Murr AH, Schindler RA. Contemporary presentation and management of a spectrum of mastoid abscesses. *Laryngoscope*. 1998;108(6):822-828. [CrossRef]
4. Saat R, Kurdo G, Laulajainen-Hongisto A, Markkola A, Jero J. Detection of coalescent acute mastoiditis on MRI in comparison with CT. *Clin Neuroradiol*. 2021;31(3):589-597. [CrossRef]
5. Platzek I, Kitzler HH, Gudziol V, Laniado M, Hahn G. Magnetic resonance imaging in acute mastoiditis. *Acta Radiol Short Rep*. 2014;3(2):2047981614523415. [CrossRef]
6. Patel KM, Almutairi A, Mafee MF. Acute otomastoiditis and its complications: role of imaging. *Oper Tech Otolayngol Head Neck Surg*. 2014;25(1):21-28. [CrossRef]
7. Thorne MC, Chewaproug L, Elden LM. Suppurative complications of acute otitis media: changes in frequency over time. *Arch Otolaryngol Head Neck Surg*. 2009;135(7):638-641. [CrossRef]
8. Schilder AGM, Chonmaitree T, Cripps AW, et al. Otitis media. *Nat Rev Dis Primers*. 2016;2(1):16063. [CrossRef]
9. Glynn F, Osman L, Colreavy M, Rowley H, Dwyer TPO, Blayney A. Acute mastoiditis in children: presentation and long term consequences. *J Laryngol Otol*. 2008;122(3):233-237. [CrossRef]
10. Psarommatis I, Giannakopoulos P, Theodorou E, Voudouris C, Carabinos C, Tsakanikos M. Mastoid subperiosteal abscess in children: drainage or mastoidectomy? *J Laryngol Otol*. 2012;126(12):1204-1208. [CrossRef]
11. Zevallos JP, Vrabec JT, Williamson RA, et al. Advanced pediatric mastoiditis with and without intracranial complications. *Laryngoscope*. 2009;119(8):1610-1615. [CrossRef]

Magnetic Resonance Findings of Dacryocystocele in an Adult: A Rare Case

Merve Kolak◍

Oral and Dental Health Training and Research Hospital, Erzincan Binali Yıldırım University, Erzincan, Türkiye

Dacryocystocele is frequently thought to be a congenital disorder and is characterized by a dilated lacrimal sac. It is an uncommon illness in adults, nevertheless. It manifests as a painless protrusion beneath the medial ligament in the medial orbital area. Its mechanism consists of an acquired obstruction at the level of Krause's valve or an obstruction at the level of Rosenmuller's valve, which is proximal to the common canaliculus.[1-3]

In this study, a rare adult case of dacryocystocele was presented with magnetic resonance (MR) images of a 59-year-old woman. After obtaining written informed consent from the patient, the MR images were presented along with the clinical data of the patient in this article.

The patient was admitted to our institutional hospital with pain in the medial orbital region. The physical examination showed swelling and erythema in this area. Additionally, there was swelling and hyperemia in the medial epicanthic folds of the orbita. There was no positive finding in specular orbital values or corneal topography metrics. Pachymetry test-corneal thickness and all biometric tests were normal. Anterior chamber and vitreous humor were within normal ranges in the examination. Physical examination also indicated a mass in the medial, naso-orbital region with a relatively dark color suspected to be cystic mass located below the medial epicanthus and canthal region, indicating a pathologic condition in the nasolacrimal sac. With gentle pressure over the mass, a mucopurulent discharge was observed. The findings were consistent with dacryocystitis, and an antibiotheraphy has been planned. Findings of the infection have regressed; however, the mass in the naso-orbital region has been still remained, and the clinicians concluded that the patient should undergo MR examination.

The MR imaging indicated a lesion with smooth contours, observed with hypointense signals in T1-weighted images and hyperintense in fat-saturated T2-weighted images. After injection of the contrast medium, there was an obvious enhancement, especially in the peripheral regions of the lesion. The radiology report revealed an infected dacryocystocele (Figures 1-4).

The differential diagnosis for a patient with nasal obstruction includes congenital bone abnormalities such as choanal atresia as well as masses like encephalocele, glioma, hemangioma, and dermoid cyst.[4,5] These medical conditions can be diagnosed by endoscopy, computed tomography (CT), MR imaging, and the tear secretion test for differential diagnosis.

Adult cases of dacryocystocele should be treated as obstructions of the nasolacrimal duct, and before undergoing external dacryocystorhinostomy, an intranasal inspection should be carried out.[6] Endoscopic marsupialization of the nasal cyst combined with stent implantation appears to be the best course of treatment, similar to what is observed in pediatric patients. External dacryocystorhinostomy is also used as another option for treatment.[7]

While congenital dacryocystocele has been identified as a distinct disease, dacryocystocele in the medial orbital region is a rather uncommon condition. Almost all cases of congenital dacryocystocele occur in pediatric individuals, and the condition has a unique natural history, set of clinical characteristics, mode of disease, and course of treatment. Both functional blockage of the common canaliculus and obstruction of the distal nasolacrimal duct promote lacrimal sac dilatation. When there is an obstruction of the nasolacrimal duct, secretions may build up in the lacrimal sac, causing it to dilate and block the common canaliculus. A second explanation for dacryocystocele is folds in the common canaliculus brought on by a dilated lacrimal sac and a malfunctioning Rosenmuller's valve as a result of inflammation and edema.[8] Antibiotics, massage, and cold compresses are used to treat children with dacryocystocele. If these treatments are insufficient, intranasal endoscopic marsupialization of the cyst along with lacrimal route probing and irrigation might be a better option.[9]
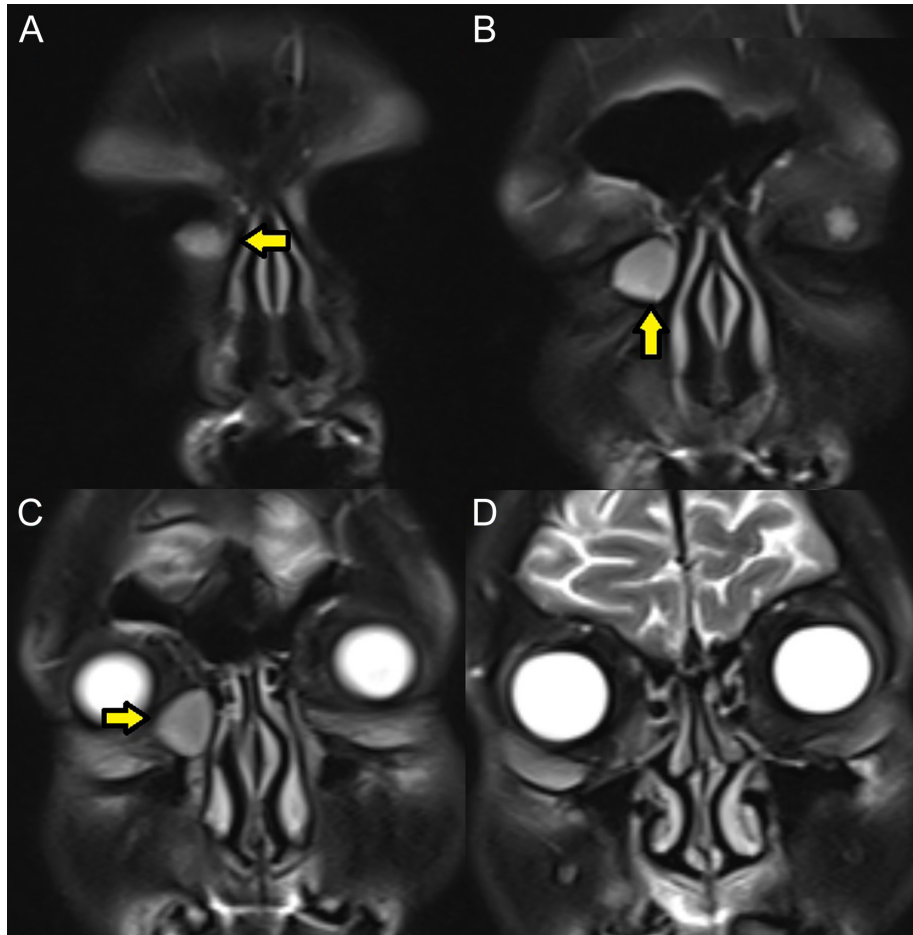
Figure 1. T2-weighted coronal plane consecutive MR images indicate the hyperintense lesion consistent with dacryocystocele (yellow arrows).

Adult cases of dacryocystocele have been reported in previous literature.[10] One of its clinical manifestations is a painless protrusion of the orbit's medial area beneath the medial ligament. The disorder can be diagnosed by MR imaging, CT, endoscopy, and the lacrimal secretion test.[11] The nasolacrimal duct blockage in adults is comparable with dacryocystocele in children regarding the mechanism of occurrence of the illness. In addition, chronic dacryocystitis is one of the complications of the dacryocystocele.[12]

Dacryocystorhinostomy and nasolacrimal stent placement have been used as treatment options for dacriocystoocele.[13] Distinguishing dacryocystocele from a lacrimal sac tumor may be essential before
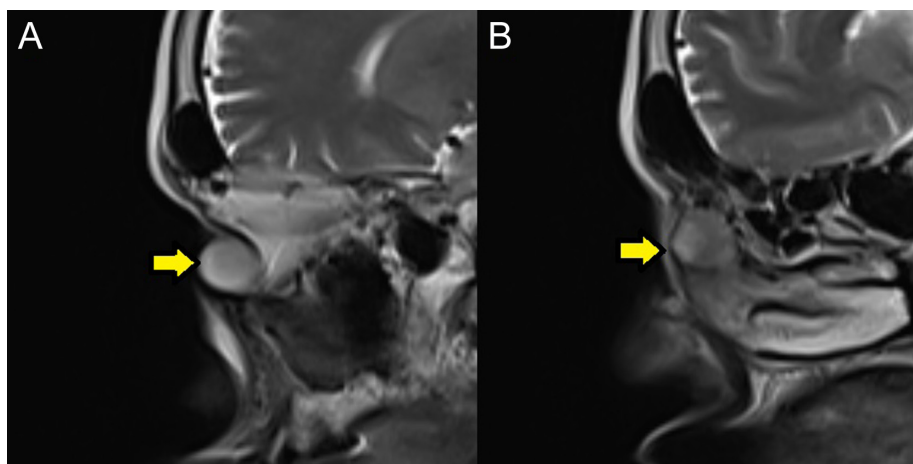
Figure 2. Sagittal plane T2-weighted MR images showing the lesion with well-defined borders (yellow arrows).
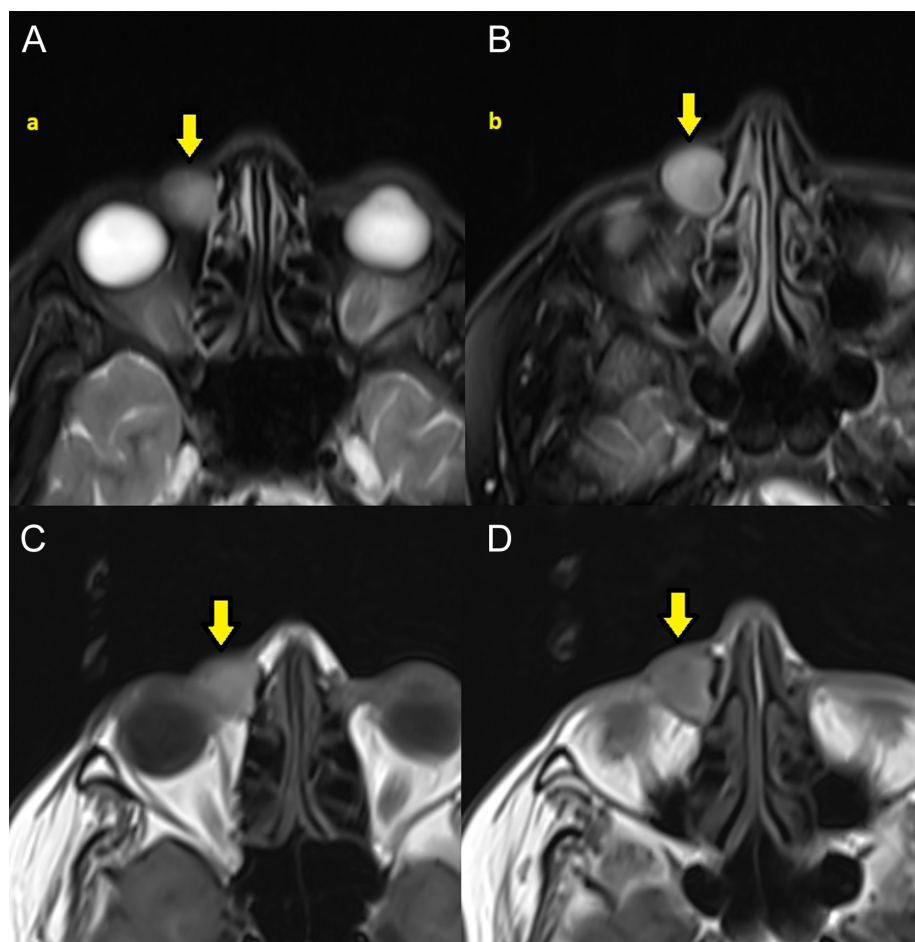
Figure 3. Axial plane T2-weighted (A, B) and axial plane T1-weighted magnetic resonance images (C, D) of the dacryocystocele (yellow arrows).
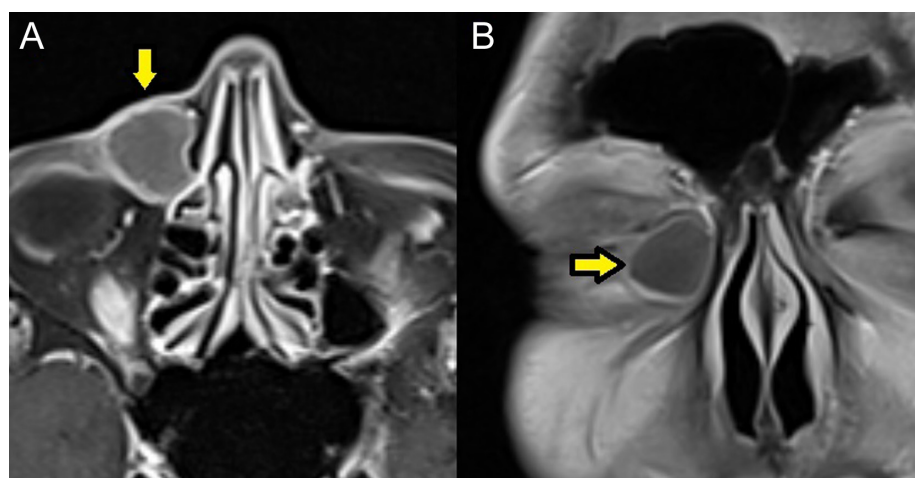
Figure 4. Axial and coronal plane enhanced T1-weighted images indicate the lesion with peripheral enhancement.

the surgical procedure.[14] Studies including CT, MR imaging, and ultrasound imaging are useful in the diagnosis of adult dacryocystocele. By displaying the dacryocystocele in the lacrimal sac and helping to distinguish it from other masses that may affect the medial canthus in adults, CT can accurately diagnose the condition anatomically. A solid mass can be observed on CT scans of orbital tumors in the medial orbital region, such as rhabdomyosarcoma, neurofibroma, lymphangioma, or hemangioma. Although CT provides a clear image of the cortical borders of the bone, MR images have also been used for this investigation to measure the lesion and

surgical planning using the superiority of this imaging modality on soft tissue contrast.

REFERENCES

1. Ansari SA, Pak J, Shields M. Pathology and imaging of the lacrimal drainage system. *Neuroimaging Clin N Am*. 2005;15(1):221-237. [CrossRef]
2. Xiao MY, Tang LS, Zhu H, Li YJ, Li HL, Wu XR. Adult nasolacrimal sac mucocele. *Ophthalmologica*. 2008;222(1):21-26. [CrossRef]
3. Lai PC, Wang JK, Liao SL. A case of dacryocystocele in an adult. *Jpn J Ophthalmol*. 2004;48(4):419-421. [CrossRef]. Accessed July 15, 2024.
4. Debnam JM, Esmaeli B, Ginsberg LE. Imaging characteristics of dacryo-cystocele diagnosed after surgery for sinonasal cancer. *AJNR Am J Neu-roradiol*. 2007;28(10):1872-1875. [CrossRef]
5. Lelli GJ, Levy RL. Epidermoid cyst masquerading as dacryocystocele: case report and review. *Orbit*. 2011;30(2):114-115. [CrossRef] Accessed July 15, 2024.
6. Day S, Hwang TN, Pletcher SD, Bhatki A, McCulley TJ. Interactive image-guided endoscopic dacryocystorhinostomy. *Ophthal Plast Recon-str Surg*. 2008;24(4):338-340. [CrossRef]. Accessed July 15, 2024.
7. Plaza G, Nogueira A, González R, Ferrando J, Toledano N. Surgical treat-ment of familial dacryocystocele and lacrimal puncta agenesis. *Ophthal Plast Reconstr Surg*. 2009;25(1):52-53. [CrossRef]
8. Rand PK, Ball WS, Kulwin DR. Congenital nasolacrimal mucoceles: CT evaluation. *Radiology*. 1989;173(3):691-694. [CrossRef]
9. Shashy RG, Durairaj VD, Holmes JM, Hohberger GG, Thompson DM, Kasperbauer JL. Congenital dacryocystocele associated with intranasal cysts: diagnosis and management. *Laryngoscope*. 2003;113(1):37-40. [CrossRef]
10. Yip CC, McCulley TJ, Kersten RC, Bowen AT, Alam S, Kulwin DR. Adult nasolacrimal duct mucocele. *Arch Ophthalmol*. 2003;121(7):1065-1066. [CrossRef]
11. Perry LJP, Jakobiec FA, Zakka FR, Rubin PAD. Giant dacryocystomu-copyocele in an adult: a review of lacrimal sac enlargements with clinical and histopathologic differential diagnoses. *Surv Ophthalmol*. 2012;57(5):474-485. [CrossRef]
12. Meyer JR, Quint DJ, Holmes JM, Wiatrak BJ. Infected congenital mucocele of the nasolacrimal duct. *AJNR Am J Neuroradiol*. 1993;14(4):1008-1010. Accessed July 15, 2024.
13. Perena MF, Castillo J, Medrano J, De Gregorio MA, Loras E, Cristo-bal JA. Nasolacrimal polyurethane stent placement: preliminary results. *Eur J Ophthalmol*. 2001;11(1):25-30. [CrossRef]
14. Sabet SJ, Tarbet KJ, Lemke BN, Smith ME, Albert DM. Granular cell tumor of the lacrimal sac and nasolacrimal duct: no invasive behavior with incomplete resection. *Ophthalmology*. 2000;107(11):1992-1994. [CrossRef]